All Theses and Dissertations

2013-07-08

The Water Entry of Slender Axisymmetric Bodies: Forces, Trajectories and Acoustics

Kyle Gordon Bodily

Brigham Young University - Provo

Follow this and additional works at: https://scholarsarchive.byu.edu/etd

Part of the Mechanical Engineering Commons

The Water Entry of Slender Axisymmetric Bodies: Forces, Trajectories and Acoustics

Kyle G. Bodily

A thesis submitted to the faculty of
Brigham Young University
in partial fulfillment of the requirements for the degree of

Master of Science

Tadd T. Truscott, Chair
R. Daniel Maynes
Julie Crockett

Department of Mechanical Engineering

Brigham Young University

July 2013

ABSTRACT

The Water Entry of Slender Axisymmetric Bodies: Forces, Trajectories and Acoustics

Kyle G. Bodily
Department of Mechanical Engineering, BYU
Master of Science

Free surface water entry of various objects has been studied using high-speed images and image processing techniques for decades. This thesis studies the forces, velocities, and trajectories of slender axisymmetric projectiles using an embedded inertial measurement unit (IMU). Three nose shapes (cone, ogive, and flat) were used in the study. Additionally, the projectiles were tested at vertical and oblique impact angles with different surface conditions. One-half of each projectile was coated down the centerline with a hydrophobic spray, creating a half hydrophobic, half hydrophilic case. The trajectory of this half-and-half case impacting vertically was compared to the trajectory of symmetrically coated projectiles impacting the free surface at oblique angles. The oblique impact cases showed significantly more final lateral displacement than the half-and-half case over the same depth. The amount of lateral displacement was also affected by the nose shape, with the cone nose shape achieving the largest lateral displacement for the oblique entry case. Instantaneous lift and drag coefficients were calculated using data from the IMU for the vertical, half-and-half, and oblique entry cases. Impact forces were calculated for each nose shape and the flat nose shape experienced impulsive forces between 25 N and 37 N when impacting vertically. The impact force for the flat nose decreased for the oblique entry case. Acoustic spectrograms showed that the sound produced during the water entry event predominately arises from the pinch-off for the cone and ogive nose shapes, with additional sound production from impact for the flat nose shape.

ACKNOWLEDGMENTS

TABLE OF CONTENTS

LIST OF TABLES

LIST OF FIGURES

NOMENCLATURE

$\mathbf{a}_i$	ith axis in initial coordinate frame
$\mathbf{a}_i'$	ith axis in first rotated coordinate frame
$\mathbf{a}_i''$	ith axis in second rotated coordinate frame
$\mathbf{b}_i$	ith axis in final coordinate frame
$\dot{\phi}$	Euler angle rate about 1st axis
$\dot{\theta}$	Euler angle rate about 2nd axis
$\dot{\psi}$	Euler angle rate about 3rd axis
ω	Angular velocity of projectile
$[R_i]$	Rotation matrix about ith axis
$[R_{kji}]$	Body-fixed rotation sequence about the ith axis, then the jth axis, then the kth axis
γ	Wetting angle
d	Distance from the nose to the center of mass
s	Sine function
c	Cosine function
$\hat{e}_i$	Unit vector along the ith axis
$\|v\|$	Magnitude of vector v
U	Total velocity of the projectile
U_o	Vertical impact velocity of the projectile
u, v, w	x, y, z components of velocity U
CoM	Center of mass
μ	Viscosity of water
D	Diameter of projectiles
σ	Surface tension of water
g	Acceleration of gravity
F_{mag}	Magnitude of the maximum impact force
IMU	Inertial measurement unit
fps	Frames per second
ρ	Density
rms	Root mean squared

CHAPTER 1.   INTRODUCTION

The splashes and cavity formation resulting from water entry have been the study of many scientists past and present and yet there remain several areas of interest to be explored. Many previous studies have focused on canonical shapes and their associated cavity dynamics, yet few authors have been able to accurately measure the accelerations and forces associated with these impacts and none have utilized an embedded accelerometer. Further, few studies have investigated acoustic signatures at impact. This thesis presents findings of the dynamics of slender axisymmetric bodies including the effects of nose shape, wetting angle, and impact angle on the object dynamics (e.g., forces, trajectory, and velocity) and cavity acoustics. This chapter presents an overview of the fundamentals of water entry, followed by a review of some of the prior work in the field of water entry of both spheres and slender axisymmetric bodies, and concludes with an overview of some of the experimental considerations used in this research.

1.1   Fundamentals of Water Entry

May et al. [1] described in detail the stages of cavity formation and collapse, and the basics will be discussed here. The splash that is observed when an object suddenly enters the water can be generalized as a two-stage process. Figure 1.1 illustrates the process for both a sphere and a slender axisymmetric body. In the *first stage*, the water on the surface is forced aside to make way for the entering body. This results in a radial sheet of water known as the splash curtain, shown in figure 1.1(a) and (e). Air is entrained behind the entering sphere as it descends, creating an air cavity below the water surface (figure 1.1(b) and (f)). The *second stage* occurs when hydrostatic forces begin to close the cavity and force pinch-off, which is the separation of the cavity into an upper and lower portion (figures 1.1(c) and (g)). Closure of the upper cavity continues and a jet of water is formed at the pinch-off point that travels through the upper cavity and beyond the water surface (figure 1.1(d) and (h)). A smaller jet is also formed in the lower portion of the cavity that
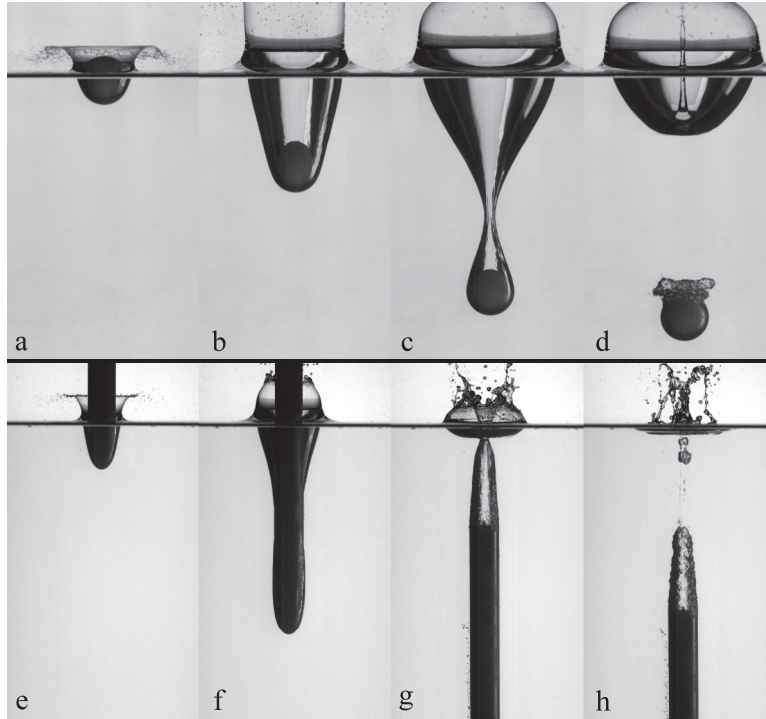
Figure 1.1: The water entry of a hydrophobic sphere (top) [3] and hydrophobic axisymmetric body (bottom) are shown. The sphere series demonstrates radial sheet formation (a), cavity formation (b), pinch-off (c), and jet formation (d). The axisymmetric body demonstrates radial sheet formation (e), pinch-off of the cavity on the body (f), pinch-off of the trailing cavity (g), and chaotic jet formation (h).

may impact on the submerged body [2]. The shape and extent of both the splash curtain and the cavity are highly dependent on the geometry of the impacting body, especially abrupt changes in geometry.

The wetting angle affects the cavity and splash formation in both the *first* and *second stage*. Figure 1.2 illustrates that when the wetting angle is greater than 90° (hydrophobic), a large cavity and initial splash form (figure 1.2(d)). Air is entrained as the object descends through the water, forming a cavity [4] (figure 1.2(e)). No cavity forms for a sphere if the wetting angle is less than 90° (hydrophilic) and only a small splash is seen due to the water flowing up and over the sphere symmetrically from all directions and colliding at the apex, forming a small jet (figure 1.2(a)). No air entrainment occurs in the hydrophilic case (figure 1.2(b)).

The different wetting angles produce similar effects for slender axisymmetric bodies. However, for the hydrophilic cases, an air cavity forms immediately behind the projectile due to the
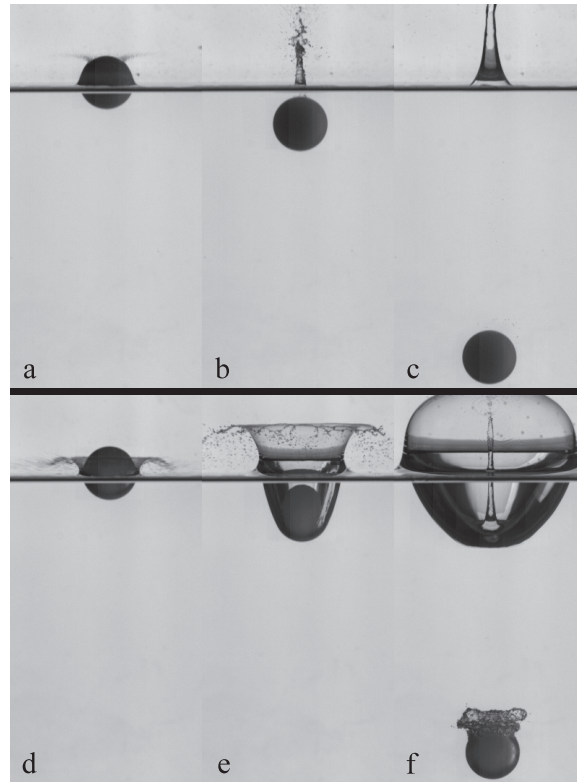
Figure 1.2: Differences in splash dynamics of hydrophilic (top) and hydrophobic (bottom) spheres [3]. For the hydrophilic sphere: (a) Initial impact. (b) Fully submerged. (c) A single jet is formed in the wake just after submergence. The hydrophobic sphere demonstrates a large splash curtain in (d) & (e) that has domed over in (f) and a jet passing through the center of the collapsing cavity towards the free surface after pinch-off.

abrupt corner, as seen in figure 1.3(b). The result is a pronounced jet that forms after pinch-off of the trailing air cavity (figure 1.3(c)), but there is no initial detached splash curtain (figure 1.3(a)). The slender axisymmetric hydrophobic case produces a splash curtain on impact as well as an open-air cavity. However, depending on the geometry of the nose and the length of the body, the splash curtain may collapse on the sides of the body (see section 3.2.1) and the pinch-off point often occurs on the side of the axisymmetric body (figure 1.1(f)), which results in a two-phase chaotic jet . The first phase (figure 1.1(g)) is due to the pinch-off of the cavity on the side of the slender axisymmetric body and the second phase (figure 1.1(h)) is from the pinch-off of the trailing cavity.
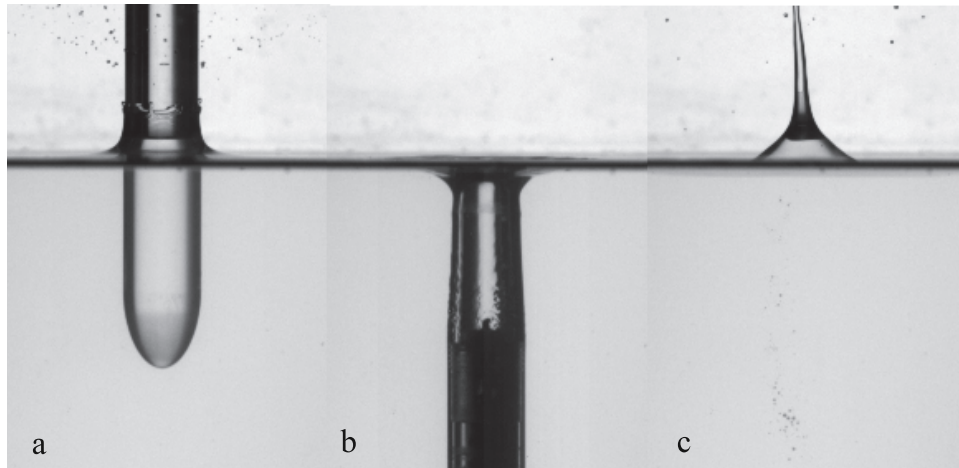
Figure 1.3: (a) Hydrophilic acrylic ogive with no splash curtain after impact. (b) Air cavity formed behind the projectile due to the abrupt corner at the tail. (c) Jet formed by the collapse of the cavity.

1.2 Background

Studies of objects entering into a liquid have been published for decades, beginning with water droplets falling into a water-milk mixture utilizing short-duration flash and hand drawing reconstruction by Worthington & Cole in 1877 [5]. Worthington then used short-duration flash photography to capture splashes in 1896 [5] and extended his studies to include cavities in 1908 [6].

A study of the comparison between the cavity dynamics of spheres and other shapes was performed by Duclaux et al. [7]. They derived an approximate analytic solution showing that there is a difference between the cavity formation of spheres and cylinders. The cavities formed by spheres were larger than the impacting sphere while the cavities formed by cylinders were roughly the same radial size as the cylinder. They showed that the cavity pinch-off time was independent of the impact velocity, but increased with an increase in diameter. They also showed that an increased diameter resulted in a decrease in pinch-off depth. Duclaux assumed a constant velocity model, but Aristoff et al. [8] expanded on the model to include acceleration changes due to hydrodynamic forces and showed that the density of a sphere significantly changed the pinch-off depth of the cavity, but the pinch-off time remained constant when compared to normalized sphere densities. Gilbarg and Anderson [9] examined the effects of atmospheric pressure on the cavity formation and collapse and showed that the cavity would remain open at the free surface permanently for pressures of 1/16 atmosphere or less. Further study of the cavity dynamics of slender axisymmetric

4

bodies and the effects of negative pressure gradients was performed by Nesteruk [10]. He used a non-linear approach to theoretically show the requirements for body geometry that would have smooth cavity closure, which would reduce drag and minimize sound generation. Lee et al. [11] used an energy dissipation model to show that the time to pinch-off was independent of impact velocity for a given projectile size, but is different for spheres, disks, etc.

The jet formation of a disk with constant velocity was studied by Gekle et al. [2]. They used a numerical simulation to show that an upper and lower jet are formed by the colliding walls from the collapsing cavity, which was also seen by Aristoff et al. [8]. Bergmann et al. [12] expanded on the work of Gekle et al. [2] by deriving a model for the radial cavity dynamics and found good agreement through experimental validation using particle image velocimetry (PIV) to compare the fluid flows. They showed that the fluid surrounding the disk interacts to force pinch-off and contributes to the jet formation seen behind the disk.

Rather than using a symmetrical surface condition for their test objects, Techet and Truscott [13] coated one hemisphere of spheres with a hydrophobic spray which resulted in the formation of an asymmetric cavity and trajectory deflection upon entering the water. These findings were similar to the results from dropping spinning spheres in the water [13] and indicated that the wetting angle could alter the trajectory of objects.

Duez et al. [4] showed that the second splash only occurs for a hydrophobic sphere and not for a hydrophilic sphere as long as the impact velocity is below about 7.5 m/s. By changing the wetting angle, they showed that viscous and capillary effects significantly controlled the cavity formation when the sphere entered the water. They also recorded the sound produced by the sphere impacts. Hydrophobic spheres resulted in a loud sound and hydrophilic spheres produced a much lower amplitude sound. The difference in sound was explained by showing that the hydrophobic spheres produced a large cavity while the hydrophilic spheres did not, and the sound results from the collapsing cavity.

Uber and Fegan [14] studied the acoustic signatures of solid metal spheres, missile-like projectiles, and bowling balls being dropped into the water. They looked at dominant frequencies, acoustic pressure, and signal decay at various impact velocities and correlated these to the kinetic energy and object shape. They showed that an object entering the water could potentially be identified by a unique frequency signature if estimates of kinetic energy or object shape can be

determined. Additional studies have been performed regarding the acoustics of water entry including a study by Honghui and Makoto [15] that measured the pressures at several distances below the free surface in the wake of a water entry projectile. They observed a somewhat uniform pressure field, with increased uniformity as distance increased from the impact location. They also showed that that the initial pressure rise occurred microseconds after the impact. Grumstrup et al. [16] noticed that cavity rippling occurs after pinch-off for spheres, hemispheres, and cones. They reported that the rippling effect is a reflected wave induced by the oscillations of the impacting body.

The study of water entry of slender axisymmetric bodies is not limited to cavity dynamics. The abrupt deceleration of high-speed bodies can cause damage, sometimes significant, to both the body and onboard instrumentation [1]. Baldwin [17] obtained simple acceleration data for cones to be used for engineering purposes. He used a single-axis crystal accelerometer to determine true velocity at impact and at subsequent times during the water entry. He used these data to determine the coefficients of drag for cone shapes at various deadrise angles as they decelerated through the water. Moghisi and Squire [18] studied the impact forces on a steel sphere at depths of up to one quarter of the sphere radius and velocities from 1 to 3 m/s.

Several numerical studies have been performed to model the water entry impact forces for both spheres and slender axisymmetric bodies. Xu et al. [19] developed a numerical simulation for the free-fall entry of cones and compared their results of acceleration and velocity to the results obtained by Baldwin, with good agreement. In 1977, Wardlaw et al. [20] used potential flow theory to develop a numerical model to predict the impact pressures and forces resulting from both vertical and oblique water entry during the initial stages. Shiffman and Spencer [21] used an integral equation model to determine the impact force of a cone and it was to these results that Moghisi and Squire [18] compared their experimental results. More recent numerical studies include hydrodynamic load prediction on two-dimensional bodies by Battistin and Iafrati [22], a shallow water entry model for small deadrise angles by Oliver [23], and an extensive numerical and experimental study of the forces experienced by both hydrophilic and hydrophobic spheres by Truscott et al. [3].

Currently, a widely used method for obtaining and analyzing the data for water entry is using high-speed imaging [4, 7, 8, 12, 13]. This method works well for observing the cavity formation and collapse, trajectory changes, and even velocities. However, using images to estimate

the accelerations of an object at impact and subsequent times will not be as precise as using a device specifically designed for the purpose of measuring acceleration. Many experimental studies of forces used accelerometers but only studied the impact event [24] [25] [18]. Advances in technology have decreased the size of the accelerometers and have enabled the construction of small embedded inertial measurement units (IMU). Tests can be performed with these embedded IMUs and the data from the impact event and subsequent times can be extracted after the experimental tests to be analyzed to show the unhindered accelerations of the test object.

1.3 Motivation and Objectives

The motivation for this research was primarily to determine how to passively control a slender axisymmetric body entering the free surface from shallow and high altitudes, to mitigate impact forces by varying the wetting angle, and to find an acoustic signature for different nose shapes. The objectives of this research were to quantitatively determine: (1) how the nose shape and asymmetric wetting angle affect the trajectory of the slender axisymmetric body, (2) how the nose shape and impact angle affect the trajectory of the slender axisymmetric body, (3) how nose shape affects the forces at impact, and (4) an acoustic signature for each nose shape at impact. These objectives were accomplished through the use of a hydrophone for sound acquisition and state-of-the-art embedded inertial measurement unit (IMU), which consists of a three-axis accelerometer and a three-axis gyroscope. Post-processing of the IMU data produced synchronized instantaneous forces, velocities, and positions throughout the impact event.

1.4 Conclusion

This chapter provided an overview of the purpose of the research and some of the basic components used in performing this research. The fundamentals of water entry were discussed including the stages of water entry ranging from impact to jet formation. Key contributors in the field of water entry have been presented with their contributions. This study used an embedded IMU and post-processing to obtain force and position data during the water entry event. Acoustic data was obtained using a hydrophone in order to determine an acoustic signature for each nose shape. The remainder of this thesis presents in detail the methods used to obtain and process the

data (chapter 2), the results and a discussion of the results (chapter 3), and the conclusions that were drawn from the results (chapter 4).

CHAPTER 2. EXPERIMENTAL METHODS

This chapter describes the equipment and procedures employed to perform the research presented in this thesis. The test apparatus and camera settings used will be described, followed by a discussion of the projectiles and their pre-test preparations. The design of and processing steps for the inertial measurement unit (IMU) will be discussed along with the synchronization method between the hydrophone and the cameras.

Each test was performed by releasing a projectile into a glass tank measuring 91.4 x 91.4 x 121.9 cm (3 x 3 x 4 ft) with water filled to 91.4 cm (3 ft). Two different heights (36 cm and 50 cm) were used to vary the impact velocity of each projectile from 2.66 m/s to 3.13 m/s. Each test was recorded at 2000 frames per second (fps) by two Photron Fastcam SA3 high-speed cameras that were positioned orthogonal to each other and normal to the tank as shown in figure 2.1(a). The resolution for each image was 512 x 768 pixels. A bank of 20 fluorescent bulbs with a diffuser sheet provided backlighting for the camera images and was placed in line with each camera behind the tank. For the vertical water entry tests, the projectile was suspended from an electromagnet by a screw that was attached to the tail of the projectile (figure 2.1(a)(A)). The projectile was released from the electromagnet after the projectile became stationary and aligned vertically. The angled water entry cases were performed by securing the projectile to a mount using a vacuum pump (figure 2.1(a)(B)). The mount was set to the appropriate angle using a three-axis positioning mechanism. The projectile dropped when the vacuum pump was turned off.

2.1 Projectiles

Acrylic, aluminum, and Delrin® acetal resin were the materials used in this study and their properties are outlined in table 2.1. The materials provided different densities and wetting angles. The nose shapes used were a cone, an elliptical ogive, and a flat nose. A profile of each nose shape is shown in figure 2.2 along with geometric parameters. The profile of the elliptical ogive

9
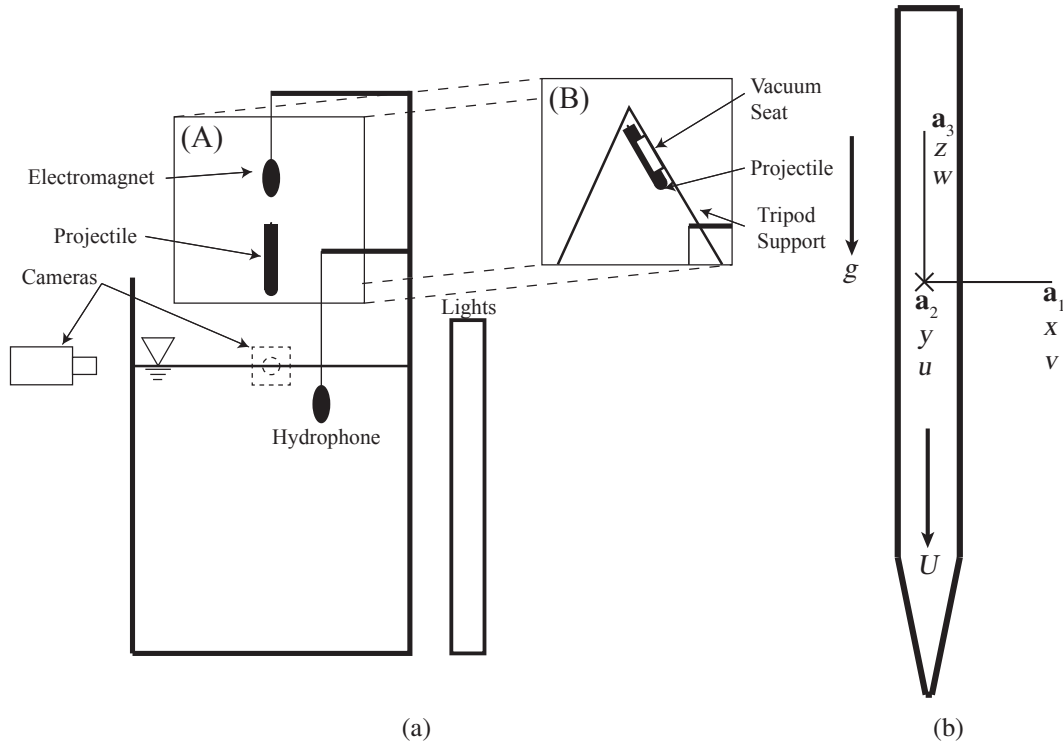
Figure 2.1: (a) Two high-speed cameras positioned at 90° around the tank captured the water entry event. A hydrophone was positioned near the impact location but out of the field of view of both cameras. (A) For vertical tests, the projectile was initially suspended from an electromagnet and then released into the tank of water. (B) Angled cases were performed by attaching a custom 1-inch-diameter grooved seat to a tripod, placing the projectile in the groove, and pulling a vacuum to secure the projectile until it was released. (b) Projectile with coordinate frame directions ($\mathbf{a}_1$, $\mathbf{a}_2$, $\mathbf{a}_3$; see section 2.5.6), position component directions (x, y, z), and velocity component directions (u, v, w). U is the total projectile velocity.

nose shape follows the function $y = (0.5in)\sqrt{1-x^2}$. The 0.4-inch section on the nose of the flat corresponds to a flat region with two 0.3-inch-radius contours on either side.

2.1.1 Projectile Surface Preparation

The surface of each projectile was prepared prior to the tests based on which case was to be performed. Immediately before each test of the hydrophilic case, the surface of the projectile was first cleansed with isopropanol and vigorously scrubbed with Kimtech Kimwipes®. More isopropanol was applied to rinse away any residual particles from the Kimwipes®. The surface

Table 2.1: Materials used in the study with wetting angles γ for both hydrophilic and hydrophobic surface conditions. The mass ratio is shown for each material-nose combination used. The Delrin center of mass (CoM) projectile was hollowed out in order to vary the location of the center of mass. The error of the wetting angle measurements is ±5°.

Material	Nose Shape	Mass Ratio	γ, Hydrophilic	γ, Hydrophobic
Acrylic	Cone	1.10	65°	120°
	Ogive	1.24	73°	119°
	Flat	1.10	79°	112°
Aluminum	Cone	2.26	64°	125°
	Ogive	2.54	62°	127°
	Flat	2.28	67°	112°
Delrin	Cone	1.27	61°	133°
	Ogive	1.42	84°	125°
	Flat	1.31	77°	108°
Delrin CoM	Ogive	1.34	84°	125°
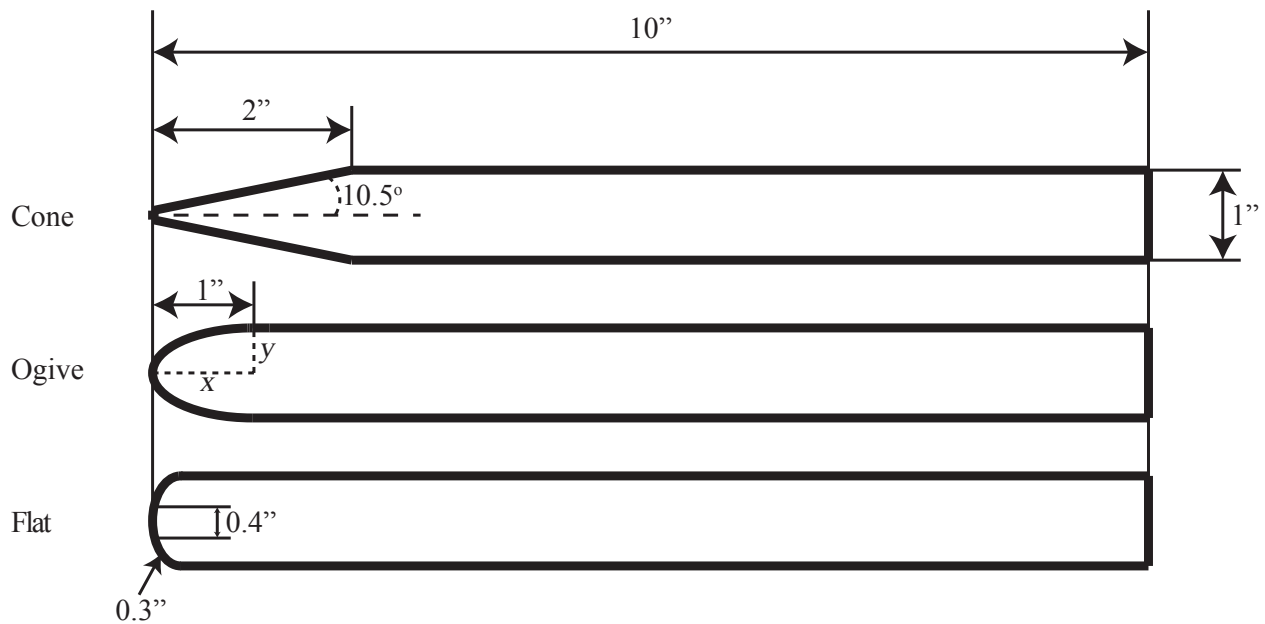
Figure 2.2: Projectiles with nose shapes used in this study. Each projectile is symmetric about the center axis.

was dried using compressed air. Ethanol was used to remove any residual film remaining from the isopropanol and to ensure that only the actual material surface contacted the water.

For the hydrophobic cases, the projectiles were cleaned using the same procedure as the hydrophilic case and then coated with Cytonix WX2100™, a hydrophobic aerosol spray. The half-and-half condition was achieved by coating only one-half of the surface along the centerline with WX2100™. The coatings were allowed to dry for at least two hours before being used in experiments. The surface properties for both the hydrophilic and hydrophobic cases for each material are shown in table 2.1. The wetting angles were measured using the procedure in section 2.1.2.

2.1.2 Measurement of Wetting Angles

The wetting angle of the nose of the projectile was determined experimentally to account for surface roughness changes from machining. High-contrast photos were taken of each nose cone on each material and the wetting angle was measured using an advancing and receding wetting angle technique. A drop was placed on the surface, a picture taken, another drop added, another picture, etc. Three drops were added and two were taken away so that the advancing and receding wetting angle could be measured. The advancing wetting angles are particularly important in this study since the projectiles entered the water from a non-wetted state. An on-screen protractor (shown in figure 2.3) was used to measure the wetting angle. In order to measure the curved surface, the protractor was rotated and visually adjusted to be normal to the surface at each edge of the droplet. Figure 2.3 also shows that the wetting angle is slightly different on the left and right sides of the water droplet. This is due do the curvature of the nose and the reported measurement is the average of the measured angle for the advancing wetting angle from both sides. The approximate average error for each wetting angle reported in table 2.1 using this method is $\pm 5°$ with a maximum average error of $\pm 11°$. The error is mostly due to positioning the protractor correctly to measure the angle of the drops.

2.1.3 Measurement of Surface Roughness

The surface roughness measurements were taken using the Hommel Tester T8000 which has a guide accuracy of 0.2 μm/60 mm [26] and a measurement resolution of 1 μm [27]. The
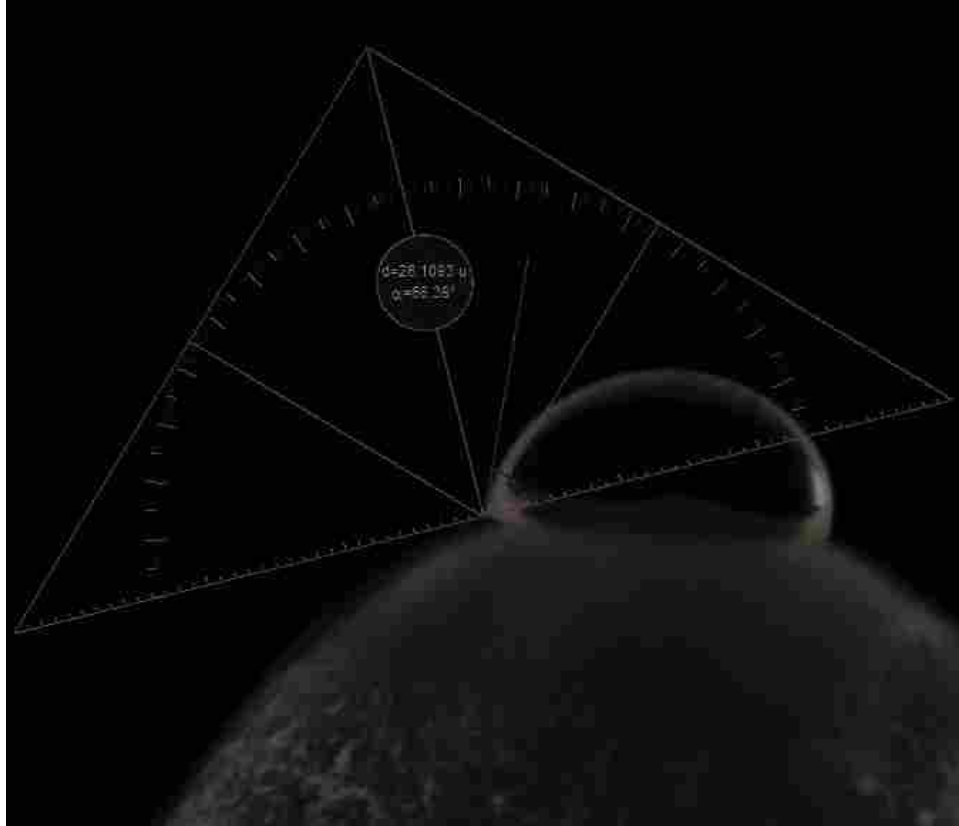
Figure 2.3: The on-screen protractor is shown during the measurement of the wetting angle of an aluminum projectile with a flat nose shape. The projectile is mounted at an angle to facilitate the placement of drops on the nose of the aluminum flat. The protractor was rotated to be normal to the surface of the projectile at the point of contact.

calibrated system has a combined variance of $\pm 3\%$ [27]. The Hommel Tester T8000 was also paired with a vibration isolation system to improve the accuracy of results, which consisted of a large granite block on top of an air bladder.

The projectile to be tested was secured at an $8°$ angle from the horizontal to enable the probe to be more orthogonal to the projectile. The projectile was oriented either in line with the translational axis of the probe for axial measurements or perpendicular to the translational axis for the radial measurements. The probe was moved a distance of 4.8 mm (0.19 in) along the surface of each projectile.

Figure 2.4 illustrates the locations for the radial and axial roughness measurements for each nose shape. For the projectiles with an ogive nose, each measurement began with the probe located 12.7 mm (0.5 in) from the constant cross section portion for axial measurements and run towards
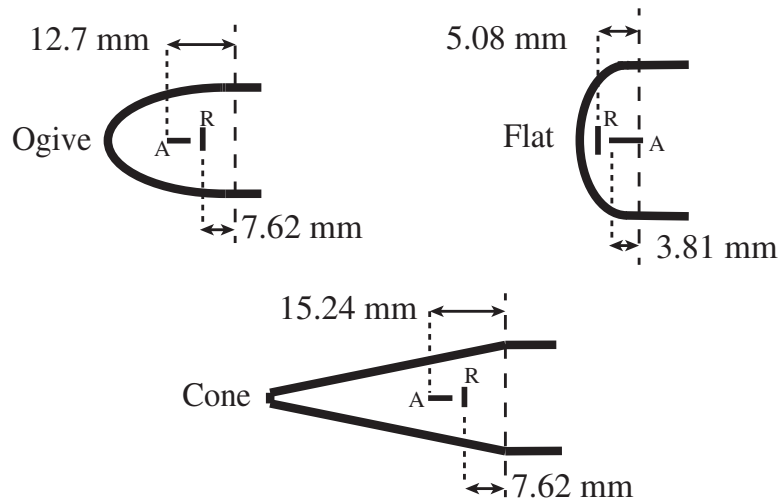
Figure 2.4: Approximate probe path for each nose shape.

the constant cross section. Similarly, the probe was started at 7.62 mm (0.3 in) for the radial direction measurements of ogive tips. For cone-shaped noses, the offset was 15.24 mm (0.6 in) in the axial direction and 7.62 mm (0.3 in) in the radial direction. Lastly, the flat-type nose offsets were 3.81 mm (0.15 in) for axial measurements and 5.08 mm (0.2 in) for radial measurements. These offsets were selected for convenience as well as enabling the measurements to be obtained closer to normal to the surface of the projectile.

In order to obtain data for both coated and non-coated projectiles, the projectiles were coated on one half of the nose and cleaned on the other half. Both sides were measured according to the above procedure. The geometry from the nose shapes was removed using a third-degree polynomial fit line to determine the contour, which was then subtracted from each measurement to obtain a flat roughness profile. Figure 2.5(a) shows a portion of the raw roughness profile points with a polynomial fit line overlaid. Figure 2.5(b) is the result of the polynomial fit subtracted from the profile points. The root mean square (RMS) roughness values for each nose are presented in table 2.2.

2.1.4   Measurement of the Center of Mass

The center of mass of each projectile was determined by balancing each projectile on the top edge of a triangular ruler. The distance from the nose of the projectile to the point of contact

14

(a)

(b)
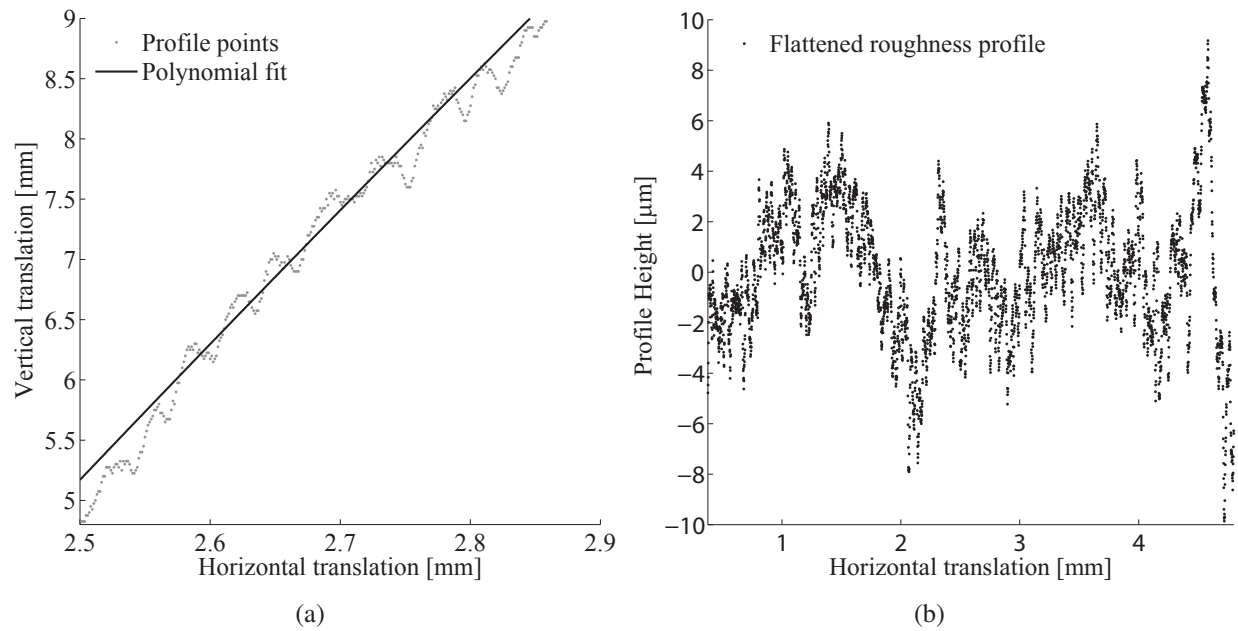
Figure 2.5: (a) Surface roughness measurements with polynomial fit line overlaid. (b) Roughness profile after removal of the projectile geometry using the polynomial fit line.

Table 2.2: Surface roughness measurements in the axial and radial directions for both hydrophilic and hydrophobic cases. The roughness RMS measurements are in μm. The uncertainty of each measurement is $\pm 3\%$.

Material	Nose Shape	Axial Philic	Axial Phobic	Radial Philic	Radial Phobic
Acrylic	Cone	0.54	2.02	0.89	2.63
	Ogive	1.54	2.32	1.14	3.00
	Flat	3.43	3.04	2.00	3.94
Aluminum	Cone	0.74	1.69	0.66	2.31
	Ogive	1.30	1.64	1.25	1.60
	Flat	1.68	2.79	0.37	2.01
Delrin	Cone	0.86	2.74	0.68	2.37
	Ogive	0.95	2.64	1.00	1.67
	Flat	1.19	4.20	1.42	3.08
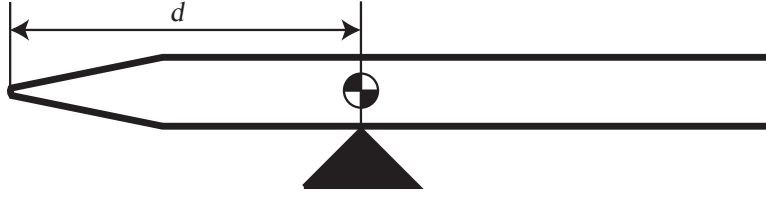
Figure 2.6: Setup for determining the location of the center of mass d of each projectile.

Table 2.3: Center of mass location d for each projectile with and without the IMU. The measurements are accurate to ± 0.05 cm.

Material	Nose	d with IMU [cm]	d without IMU [cm]
Acrylic	Cone	13.7	12.1
	Ogive	12.8	11.2
	Flat	12.4	10.7
Aluminum	Cone	12.7	12.1
	Ogive	12.0	11.3
	Flat	11.4	10.7
Delrin	Cone	13.5	12.1
	Ogive	12.5	11.2
	Flat	12.1	10.7

on the triangular ruler was measured, as shown in figure 2.6. The same procedure was performed for each projectile with the IMU embedded in the tail. The location of the center of mass of each projectile is recorded in table 2.3.

The projectile for the center of mass tests was a modified Delrin ogive and is shown in figure 2.7. A 1.91-cm (0.75-in)-diameter hole was drilled from the tail, leaving 2.54 cm (1 in) of material in the nose section. A lead slug (figure 2.7(C)) weighing 102.1 gm (0.225 lbs) and measuring 1.91 cm (0.75 in) in diameter and 3.81 cm (1.5 in) in length was used to vary the location of the center of mass of the projectile. Two spacers (figure 2.7(B) and (D)) measuring 1.85 cm (0.727 in) in diameter and 3.33 cm (1.31 in) in length were machined out of Delrin to adjust the location of the lead mass for a total of three locations. The lead slug and spacers could be arranged in different orders to change the location of the center of mass.
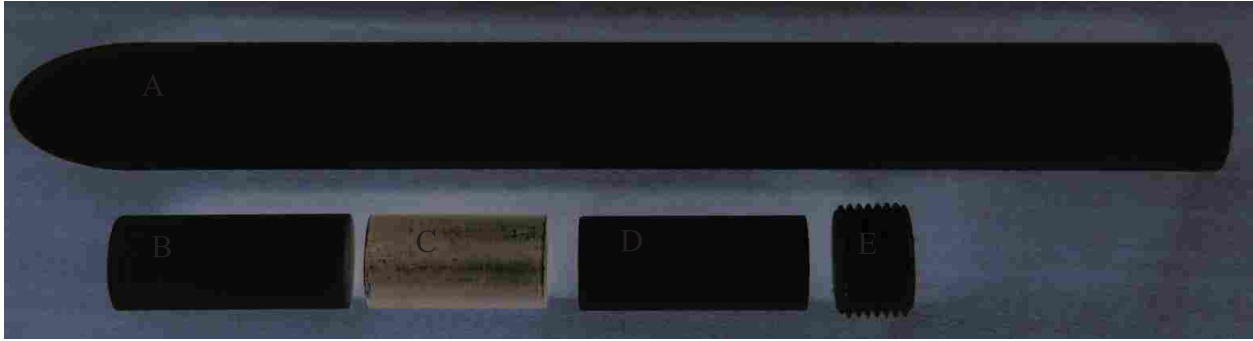
Figure 2.7: Image of the components for center of mass. (A) Modified Delrin ogive used for center of mass tests. (B) and (D) are spacers. (C) Lead slug. The order of the spacers and lead slug can be changed from BCD to CBD or BDC to vary the location of the center of mass. (E) Cap used to secure the lead slug and spacers inside the projectile.

2.2 Experimental Plan

The following tables outline the tests that were performed. Table 2.4 describes the test combinations performed for each single case. Table 2.5 describes the test combinations performed for the center of mass. Table 2.6 describes the test combinations that were performed to obtain a statistically significant set of data for a representative number of cases. Horizontal lines in the tables indicate a separate grouping of test combinations.

2.3 Dimensionless Parameters

Experiments were performed with different mass ratios and drop heights. The drop height is of special interest due to the changes in dimensionless numbers that result from the change in impact velocity. The changes to the Reynolds, Weber, and Froude numbers are shown in table 2.7. It is apparent from the very large Reynolds number that the experiment operates in the turbulent regime for both the 36-cm and 50-cm drop heights [28]. Surface tension effects at impact are negligible because the Weber number is significantly larger than 1 [29]. The Froude number is larger than 1, indicating that the inertial effects are greater than the gravitational effects.

Table 2.4: A single case for each of these combinations was performed totaling 126 tests.

Materials	Nose Shapes	Wetting Conditions	Angles	Heights
Acrylic	Cone	Hydrophilic	0°	36 cm
Aluminum	Ogive	Hydrophobic	2° ±0.1°	50 cm
Delrin	Flat		5° ±0.1°	
Acrylic	Cone	Half-and-Half	0°	36 cm
Aluminum	Ogive			50 cm
Delrin	Flat			

Table 2.5: Ten cases of each combination were performed for the center of mass tests for a total of 60 tests. The projectile for the center of mass had an ogive nose shape. Each test was dropped from 50 cm.

Wetting Conditions	Angles	CoM Location
		8.63 cm
Hydrophobic	5° ±0.1°	10.63 cm
		12.63 cm
		8.63 cm
Half-and-Half	0°	10.63 cm
		12.63 cm

Table 2.6: A series of 10 tests were performed for each of these combinations totaling 160 tests.

Materials	Nose Shapes	Wetting Conditions	Angles	Heights
	Cone	Hydrophilic	0°	50 cm
Delrin	Ogive	Hydrophobic		
	Flat			
	Cone	Half-and-half	0°	50 cm
Delrin	Ogive			
	Flat			
Aluminum	Cone	Hydrophobic	5° ±0.1°	50 cm
Delrin	Ogive			
	Flat			
Aluminum	Cone	Half-and-Half	0°	50 cm

Table 2.7: Dimensionless parameters relevant to this study at both drop heights, where $\rho = 997.88$ kg/m^3, $D = 0.0254$ m, $\mu = 0.989\mathrm{e}^{-3}$ kg·m/s, $\sigma = 0.0726$ N/m, and $g = 9.81$ m/s^2. U_o is the impact velocity.

Parameter	Equation	36 cm (U_o = 2.66 m/s)	50 cm (U_o = 3.13 m/s)
Reynolds	$\frac{\rho U_o D}{\mu}$	68,193	80,241
Weber	$\frac{\rho U_o^2 D}{\sigma}$	2470	3420
Froude	$\frac{U_o}{\sqrt{gD}}$	5.3	6.3

2.4 Electromagnet Design

The electromagnet used to suspend the projectiles for vertical impact was constructed from a 0.64-cm-diameter (0.25-in) 7.62-cm (3-in) length of steel. One end was rounded to encourage a single point of contact with the rounded screw from the tail of the projectile. A single 2-mm-diameter enameled copper wire was wound approximately 1000 times around the steel rod. The two ends of the copper wire were attached to separate terminals on a power supply and current ranging from approximately 0.7 A to 1.4 A was used to suspend the projectiles of different weights.

2.5 Inertial Measurement Unit

The IMU shown in figure 2.8 was embedded in the tail of the projectile during each test to record the instantaneous accelerations and rotation rates that the projectile experienced during the water entry event. The IMU consists of an ADXL345 accelerometer and ITG-3200 gyroscope. The accelerometer sampled at a rate of 3200 Hz, with a measurement range of ±16g, $\pm10\%$ scale factor tolerance, 0.5% nonlinearity, and a 1% cross-axis sensitivity. The gyroscope sampled at a rate of 384 Hz, with a $\pm2000°$/second measurable rate, a $\pm6\%$ scale factor tolerance, 0.2% nonlinearity, and 2% cross-axis sensitivity, and $\pm10\%$ scale factor tolerance over temperature. The temperature scale factor tolerance was important for tests where the IMU must remain embedded for long periods of time, such as before performing a $0°$ test where the projectile must become stationary and aligned perfectly vertical before proceeding with the test.

The total error the the IMU system was calculated from the manufacturer specifications to be 11.9% if temperature can be neglected, or 15.5% for worst case when the IMU is embedded
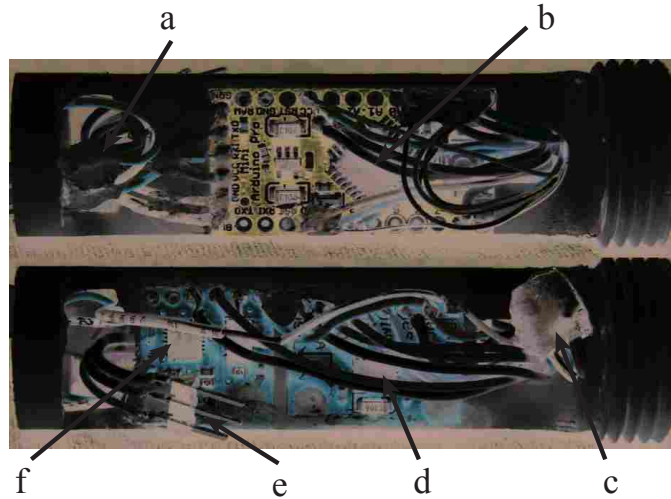
Figure 2.8: (a) Battery connection. (b) Arduino microcontroller. (c) Data flash memory. (d) ADXL345 accelerometer. (e) Data extraction connection. (f) ITG-3200 gyroscope.

for long ($>$ 2 minutes) periods of time. The total errors were calculated using the root-sum-square method.

2.5.1 Mechanical Structure and Measurement Acquisition

The ADXL345 is a capacitive accelerometer that consists of a layer of micromachined polysilicon on top of a silicon wafer [30]. The micromachined polysilicon acts as a spring that enables a mass with micro-beams to deflect different amounts when the accelerometer is subjected to accelerations. The voltage of differential capacitors that are attached to these micro-beams changes in proportion to the amount of acceleration experienced by the micro-beams, and the voltage change is measured and converted to a digital output which is recorded by the Arduino microcontroller.

The rotation rate is determined by an ITG-3200 MEMS rate gyro about three orthogonal axes based on the Coriolis Effect [31]. Capacitors attached to each axis detect the rotation in-duced by the Coriolis Effect and produce a voltage that is proportional to the rate of rotation. The detected voltage is filtered and converted to a digital value which is then passed to the Arduino microcontroller.

2.5.2 IMU Sampling Function

This section describes in detail the procedures that enabled the IMU to function.

2.5.2.1 System Start-up Behavior

On *start-up*, the device checks all attached devices for their part IDs, verifying the integrity of the communication bus and IMU functionality.

Next, the device discovers the current test number (by reading the first byte of the flash memory, which serves as the non-volatile test number pointer), and clears the block(s) of flash memory to 0xFF in a sequence that takes almost 1 second to complete. The ATmega EEPROM memory is read for the device configuration settings, such as test trigger thresholds and types. The console prompt text is printed on the UART, and global interrupts are set for the ADXL345 to trigger a sample sequence.

2.5.2.2 Main Loop

The main loops works by polling the ADXL interrupt line. If an interrupt occurs (by the ADXL345 pulling the line low), the ATmega code reads the ADXL345 Interrupt Status Register (0x30), and enters a set of *if* statements based on its contents. The individual bits/fields in the register read indicate the type of activity or event sensed by the ADXL345 which triggered the interrupt. The *if* statements are only fired if the trigger is enabled by Configuration Flag Byte that was read from EEPROM during *start-up* and is modified from the command prompt. If the function block meets the requirements, the block is executed.

For the *FreeFall*, *TwoTap*, and *OneTap if statement* blocks, the ATmega is prepared by enabling certain pins that are High-Z during sleep, and then the *Test Sample Sequence* function is called.

2.5.2.3 Sampling Sequence

The *Test Sample Sequence* function is the core piece of code-work that makes the IMU valuable. This block of pre-sampling code completely wakes the ATmega and wakes the DataFlash
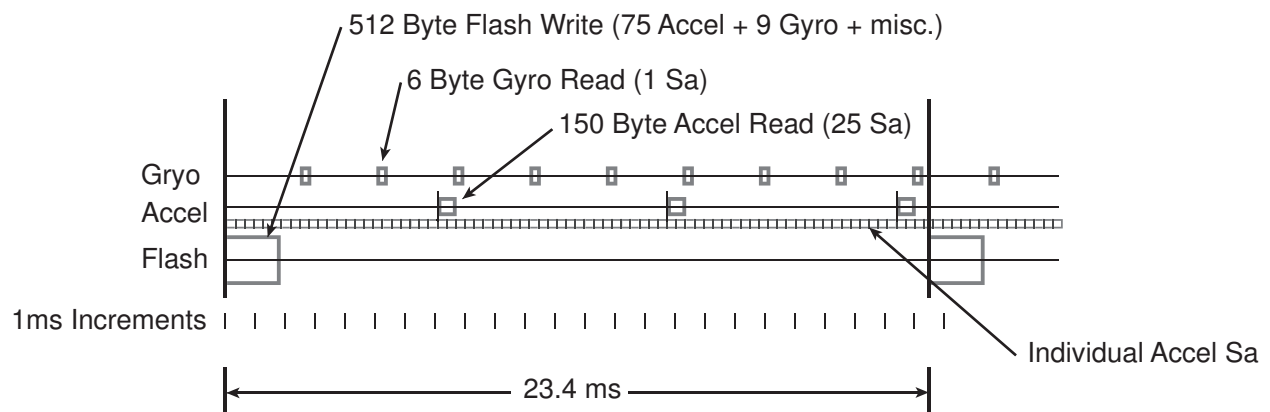
Figure 2.9: Shows the timing sequence for the sampling. The 512-byte flash write block consists of 75 accelerometer samples and 9 gyroscope samples, each containing three axes. The additional *misc.* portion contains timestamp and battery voltage information.

IC and the gyroscope. The ADXL345 is already awake to send the interrupt. After waking all parts, the ATmega records all the samples in the FIFO of the ADXL345, which represents the data set immediately before and during the event that caused the ADXL to trigger an interrupt to the ATmega. Also during this pre-sample period, the ATmega ADC is sampled several times to "pre-heat" the ADC for an accurate voltage measurement later on, as the ADC exhibits measurement artifacts in the first handful of samples it takes.

With the pre-sample actions complete, the primary loop of the *Test Sample Sequence* is entered, the timing of which is shown in figure 2.9. The set of variables involved are the *Time*, *Buffer Index Pointer*, and *Gyro Sample Index Pointer*. For each Flash Block (4096 bytes), three ADXL FIFO read dumps are taken (each dump represents 25 acceleration samples for each axis at 6 bytes per axis). While the ADXL345 accumulates samples in its internal FIFO, the ATmega takes two gyro samples. These gyro reads are timed by a polled compare in the inner loop between the ATmega TCNT1 timer and a timestamp value, which is updated on each gyro sample. A third gyro sample is started at the same time the ADXL FIFO begins a new sample set.

When the ADXL345 fills its FIFO, it signals completion with a second interrupt line to the Atmega. This line is polled in the code and, when pulled low by the ADXL345, the Atmega retrieves the 25 samples from the ADXL345 FIFO. On completing this, the code waits for the ADXL345 to de-assert the line (allow it to settle back to high), ensuring that no double-read takes

place. The process repeats three times, with the ADXL345 FIFO samples stored in a large array, and the gyro samples stored in a smaller array.

The precise sizes of the arrays are 54 bytes for the Gyro samples (three samples per FIFO dump times three FIFO dumps for each flash memory write operation, with a gyro sample consisting of three 2-byte signed integers), and 512 bytes for the ADXL345 FIFO Samples (25 samples * 3 sets per memory write operation, each sample consisting of three 2-byte signed integers, totaling 450 bytes). The *Gyro* array is added to the larger *accelerometer* array (450 + 54 = 504) and, finally, the start and stop times of the entire set are recorded in byte positions 504 and 505 for the start timestamp, and 506 and 507 for the end timestamp. The 508 and 509 bytes are the buffer index pointer, which should always read as unsigned 504. The final two bytes of the array are the battery voltage for the sample, indicating if the system was stable and within operation parameters in the same epoch as the sample set.

With the 512 byte array composed of 75 ADXL345 samples, 9 gyro samples, 2 timestamps and the check-value and system stability measurement, the array is copied over SPI to the flash memory (The Atmel DataFlash), using parity to define which of the two 512-byte buffers on the devices is used (even or odd least significant bit on the page number pointer in the Atmega). This ensures that the previous set of data which may still be in the process of being written to the flash memory is not overwritten by the new set. On completing the array write to the flash, the flash memory is commanded to write the respective buffer to the page of flash memory specified, and as this process takes place (over 6 to 10 milliseconds), the Atmega repeats the sampling loop for as many iterations as are configured.

On the end of the final iteration, the Atmega waits for the the flash memory to complete its internal write operation, and then commands the flash to reset the next set of memory blocks for the next sample call. This is done so that the flash only needs to write data without having to erase it at run-time, which is an extremely slow operation in comparison to simply writing without erasing. On cleaning out the impending test blocks, the Atmega updates the test number pointer in the first byte of flash, such that the impending test is described in non-volatile memory and is independent of the Atmega EEPROM memory, so as to preserve the test pointer even when the Atmega is reprogrammed during development. On completing all these tasks, the Atmega reports the operation on the UART for any connected serial terminal session to observe.

2.5.2.4   System Sleep

A complex power management state machine is used to control all the system devices and processor duty-cycle in an effort to reduce the power used by the logger. As the devices must remain active inside of the test projectile for several minutes in a session, and must begin capturing samples as soon as a trigger condition (normally free-fall) is detected, the state-machine is designed to keep the essential devices active while disabling the remaining devices in such a way that the system can be brought back up within milliseconds.

The prime driving mechanism for the state-machine is the *WatchDog* countdown value, an integer which is decremented each time the Atmega *WatchDog* timer rolls over. The *WatchDog* timer is a special peripheral built into the Atmega that is used to reset the processor if the code locks up or becomes unstable. The timer has a secondary function where it can be used to provide a loosely-accurate timing signal every one, two or four seconds. Each strobe of the signal decrements the countdown value.

A second peripheral, the external interrupt function, is implemented to wake the Atmega processor on any external event. The external interrupt pins are connected to the ADXL345 Interrupt lines, which allows the Atmega to go into sleep mode while the ADXL345 monitors its accelerometer for any events that characterize a trigger condition. When it detects such a condition, it pulls a configured interrupt line which wakes the Atmega. The two systems described to this point allow for the sleep behaviors to be created. The watchdog timer is a very low power device that wakes the Atmega, just like the external interrupt lines from the ADXL345, and depending on which vector initiated a processor wake event, the code will either examine the ADXL345 to discover the type of trigger event in progress, or it will decrement the watchdog countdown value. The countdown is used to keep the system active for external servicing activities such as when the user is selecting settings or retrieving samples from the devices; when the countdown reaches zero, the system enters sleep mode and saves power while waiting for a trigger event.

2.5.3   Zero-Offset Bias Removal from Accelerometer Data

It was necessary to remove the zero-offset bias from the acceleration data before performing calculations. Due to the nature of the capacitive accelerometer, the measured data should nominally
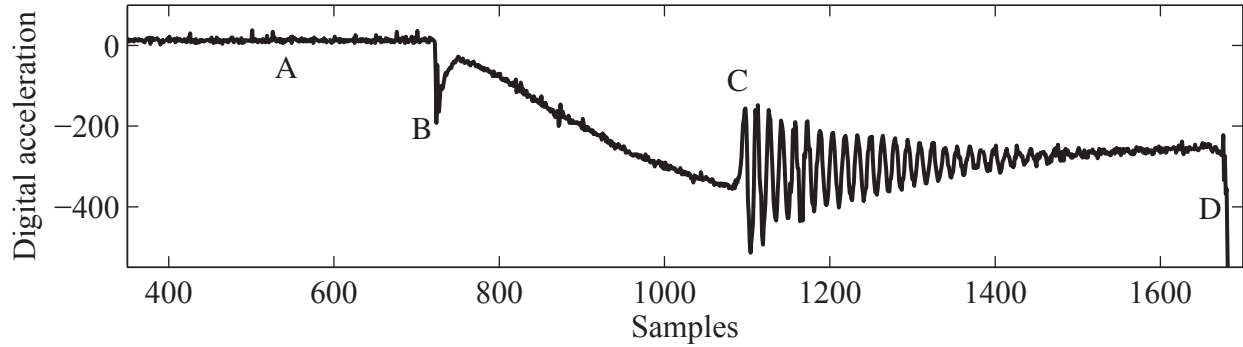
Figure 2.10: Raw acceleration data showing free-fall region (A), impact (B), pinch-off (C), and hitting the bottom of the tank (D). The vertical axis shows the digital representation of the measured accelerations as retrieved from the IMU. The horizontal axis is the sample progression.

read 0g on all axes during free-fall. Using this knowledge, the zero-offset bias was determined by calculating the mean of the free-fall portion of the data and subtracting the result from the rest of the water entry event. Figure 2.10 shows raw axial acceleration data and describes the key events. Figure 2.10(A) is a portion of the free-fall region over which the mean of the zero-offset bias is calculated.

2.5.4   Integration of Accelerometer Data

After the removal of the zero-offset bias, each measurement of the acceleration data was converted to SI units by multiplying by 0.0383 m/s^2 · bit^{-1}. The conversion factor is based on the maximum measurable acceleration value of 16g, divided by 4096 bits (the digital value corresponding to this maximum acceleration value), and then converting the 16g to m/s^2. A rotation matrix (derived in section 2.5.6) was then applied to the three-axis acceleration values at each instant in time in order to perform the integration with respect to known fixed directions. The gravity vector was applied in the vertical direction and the result was integrated numerically.

The acceleration data were integrated numerically using the trapezoidal method in MATLAB to compute velocity and then integrated again to compute position following the equation

$$\int_a^b f(x)dx \approx \frac{f(a)+f(b)}{2}(b-a),$$ (2.1)

25
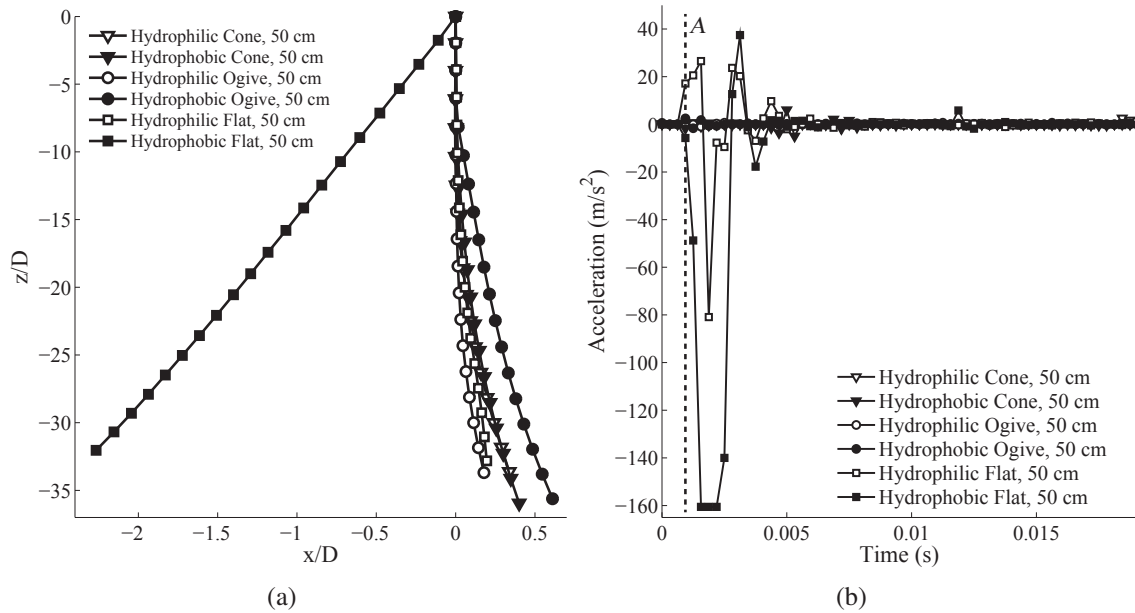
Figure 2.11: (a) The lateral trajectory of the projectile is shown throughout the descent. The hydrophobic flat case is shown to displace approximately -2.3 diameters. The large acceleration forces seen for the flat shapes are a result of the cross-axis sensitivity of the accelerometer. (b) Radial acceleration. Of note, there is no radial acceleration after these impact forces subside, indicating that the projectile is descending straight down through the water. Line *A* is the time of impact.

where a is the acceleration (or velocity) value at the first instant in time, b is the acceleration (or velocity) value at the final instant in time, and x is the incremental value between a and b.

2.5.5 Accelerometer Impact Anomaly

Numerically integrating measured acceleration data generally results in accurate position data. However, figure 2.11(a) shows that the hydrophobic flat-nosed projectile with no initial entry angle had a lateral displacement of -2.2 diameters. Comparing the computed position from the IMU with the position estimated using the images shows that the computed IMU position is grossly inaccurate. It is clear from figure 2.12(a) that there is less than one-half diameter lateral displacement from impact until the projectile leaves the image frame. The discrepancy is due to a large initial impulsive force experienced by the IMU upon impact.

The blunt geometry of the flat is responsible for the impulsive acceleration that is significantly higher for the flat than for the cone or ogive geometries. The impulsive acceleration
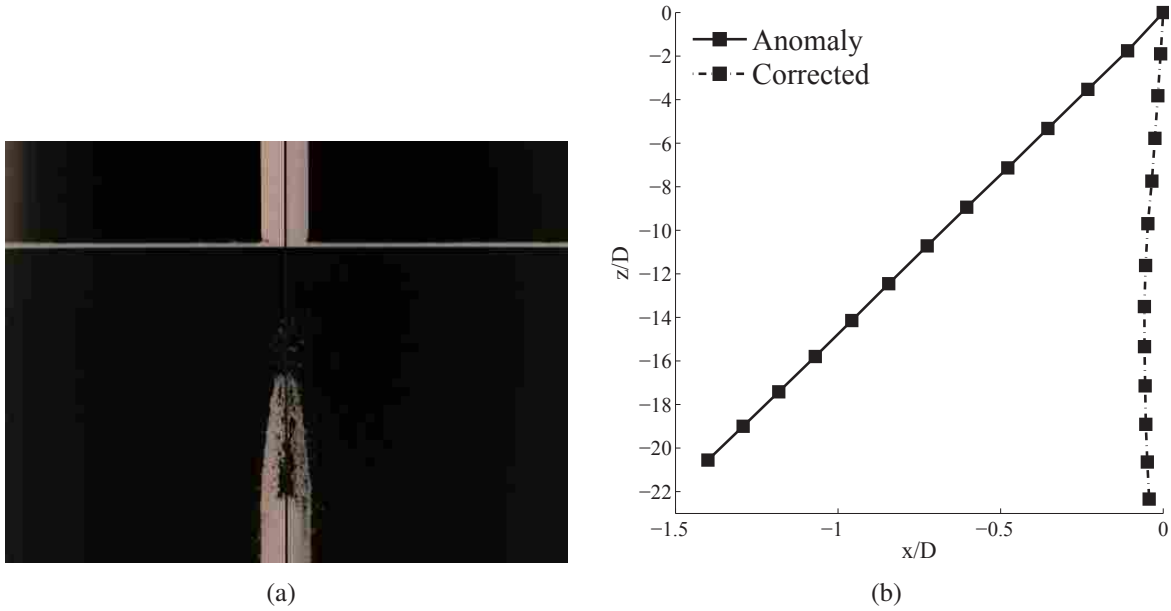
Figure 2.12: (a) Combined image of the projectile at impact and leaving the frame. A vertical line shows that little lateral position displacement is observable on images. (b) The *Anomaly* plot is the calculated position from the IMU if the impact acceleration is included. A lateral displacement of -1.4 diameters is seen over the same time interval as (a). The *Corrected* plot shows a lateral displacement of -0.04 diameters after the removal of the impact acceleration anomaly.

reaches the maximum measurable value of the accelerometer (160 m/s^2). Cross-axis sensitivity is a mechanical property of the accelerometer where an acceleration from one axis can induce accelerations on the other two axes. Figure 2.11(b) presents the radial acceleration component for cone, ogive, and flat nose shapes. The two acceleration plots for the flat nose shape shows significant acceleration at impact A, which are not seen for the cone and ogive nose shapes. The large impulsive acceleration experienced at impact along the axial axis of the projectile induced an acceleration along the radial axis. Using a Butterworth low-pass filter with a cutoff frequency of 50 Hz removed the impulsive acceleration experienced by the projectile and results in an accurate trajectory plot, shown in figure 2.12(b).

2.5.6 Gyroscope Data Processing

A gyroscope was used to relate the orientation of the accelerometer axes at each instant to the initial orientation in order to calculate the components of acceleration in the vertical and horizontal directions. The following derivation results in a transformation matrix $[B]$ that relates

$$[R_3(\psi)] \qquad [R_2(\theta)] \qquad [R_1(\phi)]$$

(a)   (b)   (c)   (d)
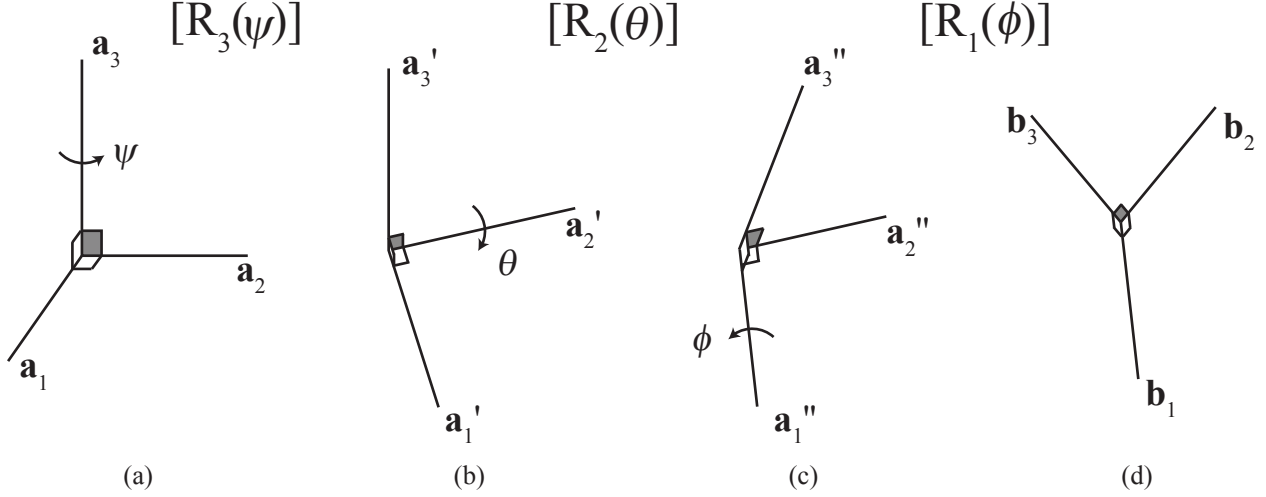
Figure 2.13: Sequence of rotated coordinate frames. (a) Initial frame is rotated by $[R_3(\psi)]$ to achieve (b), which is rotated by $[R_2(\theta)]$ to (c), and finally rotated by $[R_1(\phi)]$ to achieve the final frame (d).

the simultaneous three-axis rotation measurements from the gyroscope to the component rotations about each axis of the body-fixed coordinate frame. The Euler angle transformation was performed using a body-fixed 3-2-1 rotation sequence [32], shown in figure 2.13. Each frame is rotated by the corresponding $[R]$ matrix to achieve to next frame. Rotations around the body-fixed 1, 2, and 3 axes are ϕ, θ, and ψ, respectively, and are called the Euler angles. The individual rotation matrices used for each stage in the rotation sequence are

$$\left[R_3\right] = \begin{bmatrix} c\psi & s\psi & 0 \\ -s\psi & c\psi & 0 \\ 0 & 0 & 1 \end{bmatrix} \qquad \left[R_2\right] = \begin{bmatrix} c\theta & 0 & -s\theta \\ 0 & 1 & 0 \\ s\theta & 0 & c\theta \end{bmatrix} \qquad \left[R_1\right] = \begin{bmatrix} 1 & 0 & 0 \\ 0 & c\phi & s\phi \\ 0 & -s\phi & c\phi \end{bmatrix}. \qquad (2.2)$$

Pre-multiplying the individual rotation matrices from equation set 2.2 in the correct 3-2-1 sequence yields a total transformation matrix to express the current orientation in terms of the previous orientation,

$$\left[R_{123}\right] = \left[R_1\right]\left[R_2\right]\left[R_3\right] = \begin{bmatrix} c\psi c\theta & s\psi c\theta & -s\theta \\ -s\psi c\phi + c\psi s\theta s\phi & c\psi c\phi + s\psi s\theta s\phi & c\theta s\phi \\ s\psi s\phi + c\psi s\theta c\phi & -c\psi s\phi + s\psi s\theta c\phi & c\theta c\phi \end{bmatrix}. \qquad (2.3)$$

A relationship must be found to relate ϕ, θ, and ψ to the small amount of rotation each axis undergoes at each time step. The instantaneous angular velocities ω_1, ω_2, and ω_2, measured from each axis of the gyroscope, are combined into the total instantaneous angular velocity ω which is equated to the components of the Euler angle rates $\dot{\phi}$, $\dot{\theta}$, and $\dot{\psi}$ that occur from each transformation. This equation is presented in equation 2.4 as

$$\omega = \dot{\psi}\mathbf{a}_3 + \dot{\theta}\mathbf{a}_2' + \dot{\phi}\mathbf{a}_1'', \tag{2.4}$$

where $\mathbf{a}_3$ is the third-axis unit vector in the initial coordinate frame (figure 2.13(a)), $\mathbf{a}_2'$ is the second-axis unit vector in the first rotated coordinate frame (figure 2.13(b)), and $\mathbf{a}_1''$ is the first-axis unit vector in the second rotated frame (figure 2.13(c)). Currently, the unit vectors are expressed in terms of their respective coordinate frames, but they must be expressed in a common frame to be used in subsequent calculations. Equation 2.5a expresses the axes of the final coordinate frame $\mathbf{b}_i$ in terms of the initial frame $\mathbf{a}_i$. Equation 2.5b expresses the axes of the final coordinate frame $\mathbf{b}_i$ in terms of the first rotated frame $\mathbf{a}_i'$. Equation 2.5c expresses the axes of the final coordinate frame $\mathbf{b}_i$ in terms of the second rotated frame $\mathbf{a}_i''$.

$$\left[R_{123}\right] = \begin{bmatrix} c\psi c\theta & s\psi c\theta & -s\theta \\ -s\psi c\phi + c\psi s\theta s\phi & c\psi c\phi + s\psi s\theta s\phi & c\theta s\phi \\ s\psi s\phi + c\psi s\theta c\phi & -c\psi s\phi + s\psi s\theta c\phi & \underbrace{c\theta c\phi}_{\mathbf{a}_3} \end{bmatrix} \tag{2.5a}$$

$$\left[R_{12}\right] = \begin{bmatrix} c\theta & 0 & -s\theta \\ s\phi s\theta & c\phi & c\theta s\phi \\ c\phi s\theta & \underbrace{-s\phi}_{\mathbf{a}_2'} & c\phi c\theta \end{bmatrix} \tag{2.5b}$$

$$\left[R_1\right] = \begin{bmatrix} 1 & 0 & 0 \\ 0 & c\phi & s\phi \\ \underbrace{0}_{\mathbf{a}_1''} & -s\phi & c\phi \end{bmatrix} \tag{2.5c}$$

The rotation matrices are orthogonal so $[R]^{-1} = [R]^T$. The body-fixed unit vectors can be obtained from the respective columns of the rotation matrices from each frame and are expressed in the unit vectors of the final frame $\mathbf{b}_1$, $\mathbf{b}_2$, and $\mathbf{b}_3$, written as

$$\mathbf{a}_3 = -s\theta \mathbf{b}_1 + c\theta s\phi \mathbf{b}_2 + c\phi c\theta \mathbf{b}_3 \tag{2.6a}$$

$$\mathbf{a}_2' = c\phi \mathbf{b}_2 - s\phi \mathbf{b}_3 \tag{2.6b}$$

$$\mathbf{a}_1'' = \mathbf{b}_1 \tag{2.6c}$$

Substituting the unit vector components from equation 2.6 into equation 2.4 and combining similar terms results in

$$\omega = (-\dot{\psi}s\theta + \dot{\phi})\mathbf{b}_1 + (\dot{\psi}c\theta s\phi + \dot{\theta}c\phi)\mathbf{b}_2 + (\dot{\psi}c\theta c\phi - \dot{\theta}s\phi)\mathbf{b}_3. \tag{2.7}$$

Expressing equation 2.7 in matrix form yields

$$\underbrace{\begin{bmatrix} \omega_1 \\ \omega_2 \\ \omega_3 \end{bmatrix}}_{\{\omega\}} = \underbrace{\begin{bmatrix} -s\theta & 0 & 1 \\ c\theta s\phi & c\phi & 0 \\ c\theta c\phi & -s\phi & 0 \end{bmatrix}}_{[B]} \underbrace{\begin{bmatrix} \dot{\psi} \\ \dot{\theta} \\ \dot{\phi} \end{bmatrix}}_{\{\dot{\theta}\}}, \tag{2.8}$$

where $[B]$ is the transformation matrix from the known Euler angle rates to the instantaneous angular velocities. The Euler angle rates can be obtained by multiplying by $[B]^{-1}$ on each side, yielding

$$\begin{bmatrix} \dot{\psi} \\ \dot{\theta} \\ \dot{\phi} \end{bmatrix} = \begin{bmatrix} 0 & \frac{s\phi}{c\theta} & \frac{c\phi}{c\theta} \\ 0 & c\phi & -s\phi \\ 1 & \frac{s\phi s\theta}{c\theta} & \frac{c\phi s\theta}{c\theta} \end{bmatrix} \begin{bmatrix} \omega_1 \\ \omega_2 \\ \omega_3 \end{bmatrix}. \tag{2.9}$$

The Euler angle rates can be separated into individual components for convenience as follows

$$\dot{\psi} = \frac{1}{cos\theta}(\omega_2 s\phi + \omega_3 c\phi) \tag{2.10a}$$

$$\dot{\theta} = \omega_2 c\phi - \omega_3 s\phi \tag{2.10b}$$

$$\dot{\phi} = \frac{1}{cos\theta}(\omega_2 s\theta s\phi + \omega_3 s\theta c\phi) + \omega_1, \tag{2.10c}$$

with a singularity seen in equations 2.10a and 2.10c when $\theta = \pm 90°$. The 3-2-1 rotation sequence was selected due to this singularity as opposed to having a singularity at $\theta = 0°, \pm 180°$ that occurs when using other rotation sequences and was necessary because the initial state of a portion of the experiment occurred at $\theta = 0°$.

The Euler angle rates in equation 2.10 can be integrated at each time step and the computed Euler angles ϕ, θ, and ψ can be substituted into equation 2.3 to obtain the rotation for the current time step. The current orientation can be expressed in terms of the initial orientation by post-multiplying successive rotation matrices.

An additional step was necessary to correctly orient the coordinate frames for the oblique cases relative to the gravity vector. Using another 3-2-1 body-fixed rotation sequence, the $\mathbf{a}_3$ axis of the coordinate frame was transformed from the vertical direction to the initial angle of $2°$ or $5°$. This transformation results in the same rotation matrix as equation 2.3. The third column of equation 2.3 describes the direction cosines between each transformed $\mathbf{b}_1$, $\mathbf{b}_2$, and $\mathbf{b}_3$ axis and the original $\mathbf{a}_3$ axis, shown in figure 2.14. The acceleration components measured by the accelerometer in the initial angled state were used to determine the orientation of the IMU relative to gravity. The angles α_1, α_2, and α_3 were determined using the geometric definition of the dot product (equation 2.11a), with the knowledge that $\hat{e}_i$ is the direction unit vector corresponding to the ith axis of the accelerometer and the magnitude of the gravity vector $\hat{G}$ is the square root of the sum of the squared acceleration components, shown in equation 2.11b where g_i is the acceleration due to gravity in the ith direction.

$$\hat{e}_i \cdot \hat{G} = \|\hat{e}_i\|\|\hat{G}\|cos\alpha_i \tag{2.11a}$$

$$\alpha_i = cos^{-1}\frac{g_i}{\sqrt{g_1^2 + g_2^2 + g_3^2}} \tag{2.11b}$$

The cosine of angles α_1, α_2, and α_3 were equated to their respective elements from the third column of equation 2.3 to compute the rotation about each axis from the 3-2-1 transform of the
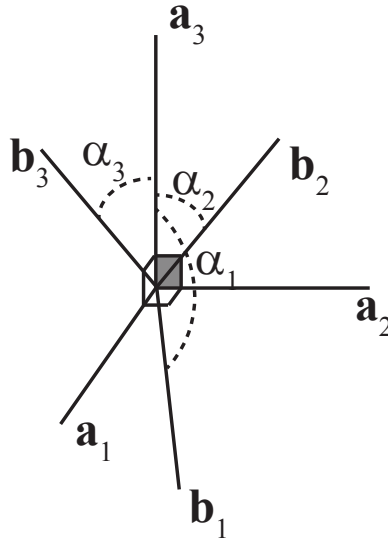
Figure 2.14: Angles between the final transformed axes and the initial vertical axis used to relate the coordinates to gravity.

oblique cases. Solving for ϕ, θ, and ψ yields the angles

$$\theta = sin^{-1}\left(-cos\alpha_1\right) \tag{2.12a}$$

$$\phi = cos^{-1}\left(\frac{cos\alpha_3}{cos\theta}\right) \tag{2.12b}$$

$$\psi = 0, \tag{2.12c}$$

which were used in equation 2.3 to solve for the transformation matrix from vertical to the initial angle relative to the known gravity vector. The inverse of the transformation matrix was applied to the rotation matrix at each time step in order to correctly apply the gravity vector before integrating and calculating the velocity and trajectory of the projectile.

2.5.7 IMU Validation

The validity of the IMU measurements and the code used in the analysis procedure were also obtained. A pendulum validation mechanism was created because of the similarity between the circular arc and the curving that was expected that the projectile would undergo in the actual experiments. The IMU was embedded in a projectile and the two were secured to the pendulum
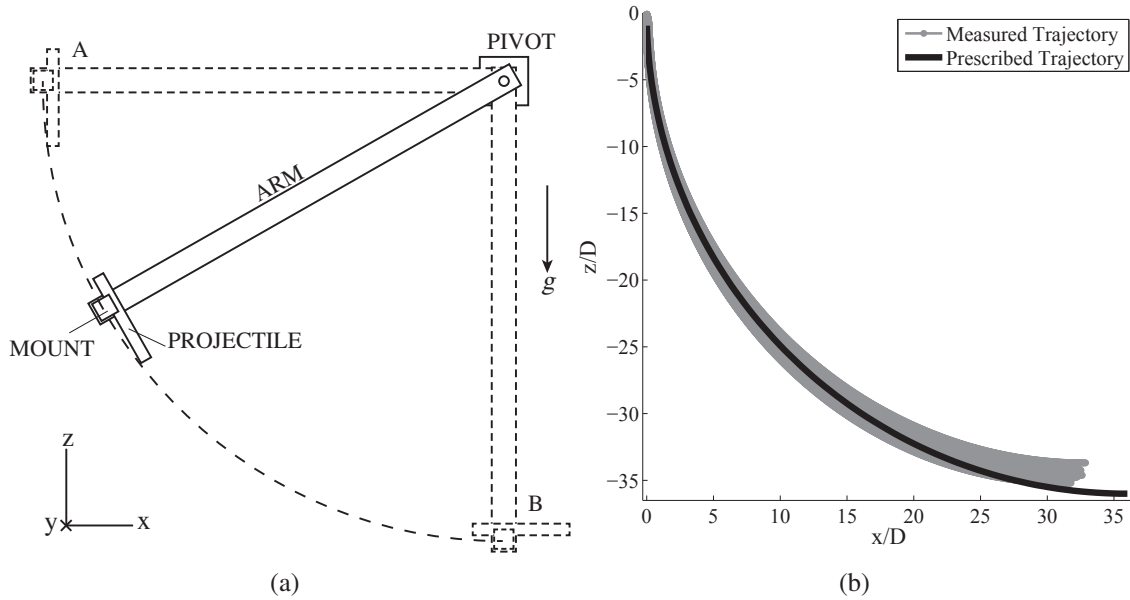
Figure 2.15: (a) Line drawing of the mechanism used for IMU validation tests. (b) Measured trajectories for 20 tests compared to the prescribed trajectory of a quarter circle with a radius of 36 inches.

arm such that the actual accelerometer chip was located along the centerline of the pendulum arm at a distance of 36 inches from the pivot point. Figure 2.15(a) shows the validation setup in the initial (A) and final (B) test locations as well as an intermediate position. The results of 20 validations tests are compared to the prescribed trajectory of a quarter circle with a radius of 91.44 cm (36-in), shown in figure 2.15(b). The error between the final measured point and the final prescribed point was calculated by subtracting the distance between the two final points and dividing by the prescribed final point distance. The total mean IMU error was calculated from the mean of 20 tests to be 11.6%, with a standard deviation of 0.68%. The error value is within the total error calculated from the manufacturer specifications discussed previously.

2.6 Hydrophone Processing Methods

The hydrophone was positioned 26 cm (10.25 in) from the impact location, which was as far from the walls of the tank as possible while still being out of the field of view of both cameras. The horizontally omnidirectional hydrophone has a sensitivity of -180dB and a useful range of 10 Hz to 100 kHz [33]. It was connected to a computer using a standard 3.5-mm microphone input

33

and the signal coming from the hydrophone was recorded using Audacity software at a rate of 96 kHz, which provided a maximum measurable frequency of one-half the sampling rate (48 kHz) according to the Nyquist sampling theorem [34].

2.6.1 Hydrophone-Camera Synchronization

The hydrophone data and the images were synchronized by utilizing the record state output from the Photron Fastcam SA3 cameras. This record state signal was connected to one channel of the stereo microphone input and the hydrophone signal was connected to the other stereo input. This configuration ensured that the hydrophone samples were obtained at a known time relative to the images from the camera. The camera record state output signal was set to be high (5 volts) when not recording and low (0 volts) when recording so as to remove any overlap with the hydrophone signal. The camera trigger mode was set to center trigger and the impact image frame number was converted to hydrophone time by taking half of the time that the camera was capable of recording (0.9075 s), calculating the frame corresponding to this time, and subtracting the time of the impact image from the time of the center image. The error associated with this method is ±0.25 ms due to the 2000 fps used as the camera framerate.

2.6.2 Spectrogram Processing

The synchronized data were processed over the portion of the hydrophone data containing the impact and pinch-off events using the MATLAB spectrogram function. The instant of impact was used as the reference point and 0.1 s of data was included before the impact event and 0.25 s of the data was included post-impact. Including some of the data beyond the actual water entry event was necessary for calculations involving fast Fourier transforms (FFT). The spectrogram calculations were performed using a Hanning window size of 512 with 250 samples of overlap. Using overlapping samples produces a smoother spectrogram than if no overlap is used.

Figure 2.16 demonstrates the effect of different window sizes. Larger windows are capable of resolving a wider range of frequency values, but more samples are needed and the resulting plot is significantly distorted in time. The windows size of 512 samples results in a spectrogram that has better time resolution at the expense of frequency resolution when compared to larger window

Table 2.8: Sizes for the Hanning window used in calculating the spectrograms along with the respective frequency resolution and time resolution.

Window Size	Frequency Res. [Hz]	Time Res. [ms]
512	187.5	5.3
4096	23.4	42.7

sizes. A window size of 4096 was used to calculate the frequencies for the impact and pinch-off events in section 3.4. Using the larger window size produced plots with finer frequency resolution. Table 2.8 presents the two window sizes used in processing the data with their respective time and frequency resolution values. The frequency resolution was computed by the equation

$$f_{res} = \frac{F_s}{N},\tag{2.13}$$

where F_s is the sampling frequency and N is the number of samples per window. The time resolution is simply the reciprocal of the frequency resolution and defines the time step between chunks of frequency values through time.

2.7 Conclusion

This chapter described the experimental setup and processing techniques used in performing the research presented in chapter 3. The projectile parameters and tests performed were provided as well as a description of the test procedure. The sampling method used by the IMU obtain the data was explained. A method for validating the position output from the IMU was described and the derivation of the gyroscopic transformations necessary to accurately compute the position were presented. Finally, a description of the synchronization and processing used for the acoustic data was provided.

(a) Size = 128. (b) Size = 512. (c) Size = 1024.

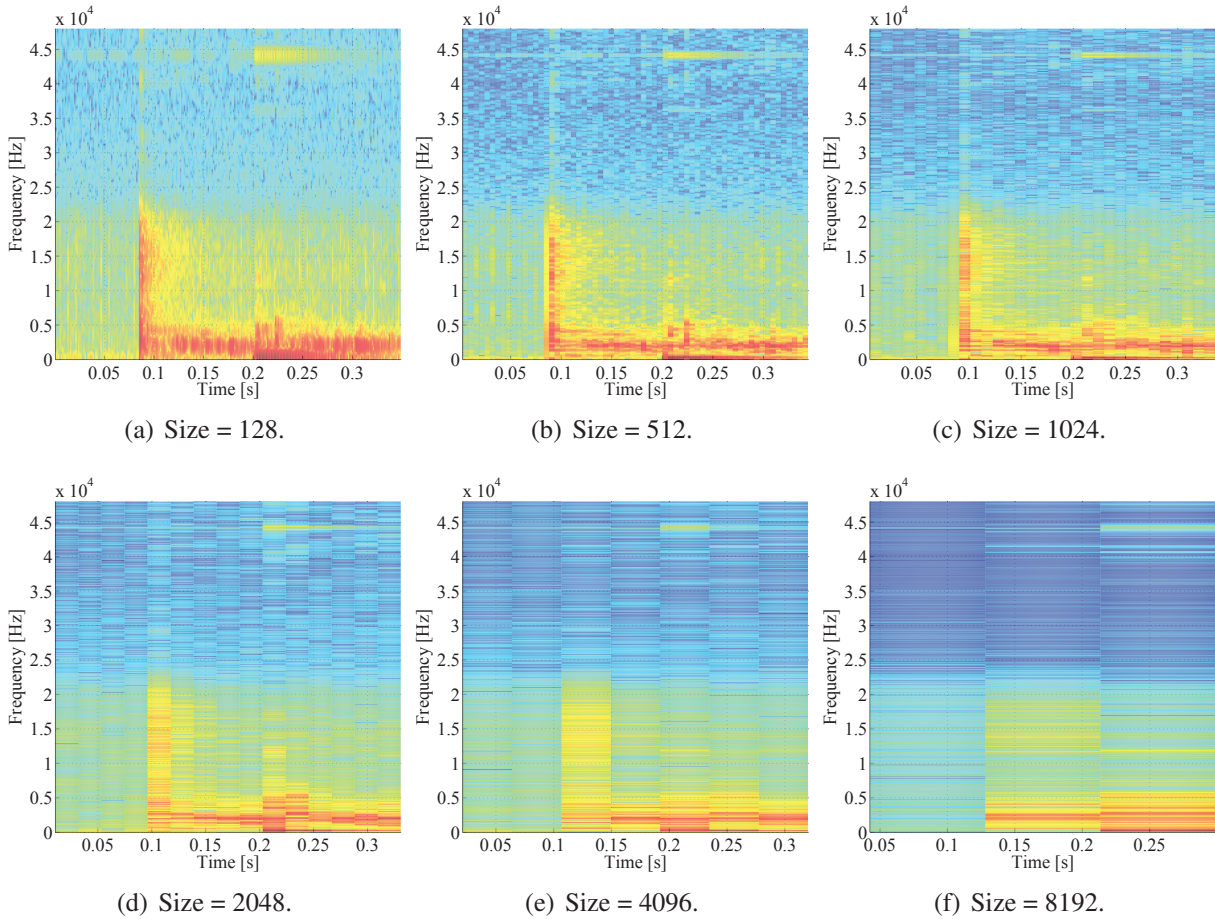(d) Size = 2048. (e) Size = 4096. (f) Size = 8192.

Figure 2.16: Comparison of different possible window sizes for computing the spectrogram. Time resolution is greatest for the smallest window (a) and frequency resolution is greatest for the largest window (f).

CHAPTER 3.   RESULTS AND DISCUSSION

This chapter presents a discussion of the results for the tests performed from tables 2.4 through 2.6. A single test was performed for all 126 unique cases outlined in table 2.4, which consisted of combinations of acrylic, aluminum, and Delrin materials with cone, ogive, and flat nose shapes performed with three different surface conditions and three different impact angles. Additionally, the 16 cases from table 2.6 were repeated 10 times to use for statistical comparison. The 6 cases for the center of mass experiments (table 2.5) were also performed 10 times each. The results will be presented in sections beginning with trajectory and velocity considerations, followed by force considerations, and finally a discussion of the some of the acoustics of the water entry event.

3.1   Acceleration Data

Figure 3.1(a) presents an image sequence of a hydrophobic Delrin ogive impacting the free surface at $5°$ with a velocity U_o of 3.13 m/s. Figure 3.1(b) shows the axial acceleration measurements. The impact of the projectile caused an acceleration spike (A), followed by a gradual increase in acceleration until pinch-off of the main cavity occurred on the side of the projectile (B) and at pinch-off of the trailing cavity (C). The oscillations immediately following C will be discussed in section 3.4.1. There was only a very small disturbance in the radial accelerations at impact, shown in figures 3.1(c) and 3.1(d), indicating that most of the impact acceleration occurred in the axial direction due to the completely vertical velocity and projectile orientation. Both figures 3.1(c) and 3.1(d) show pronounced accelerations during the on-body pinch-off (B), but did not measure any accelerations for the pinch-off of the trailing cavity (C).
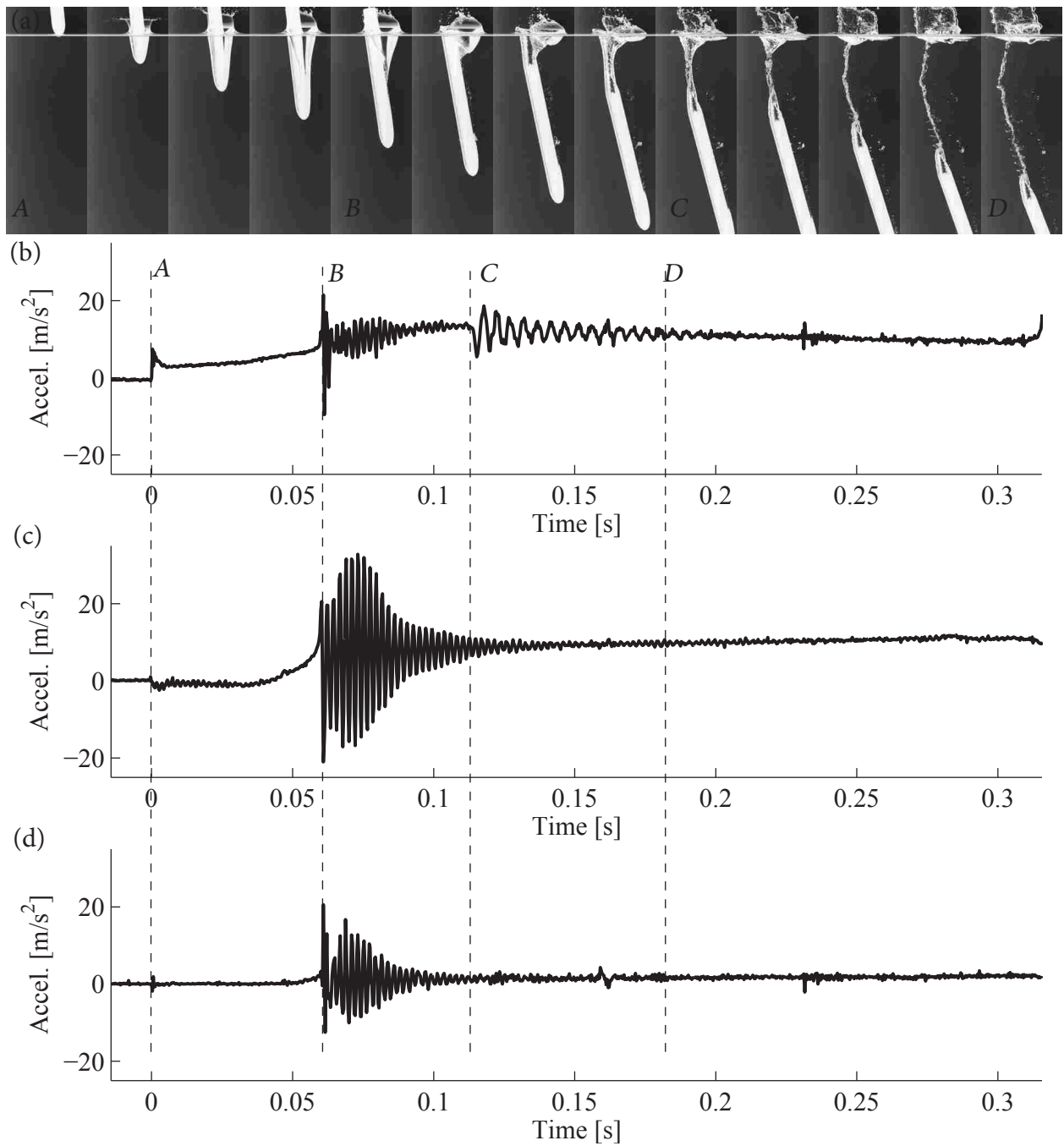
Figure 3.1: Acceleration data correlated in time to images. (a) Image sequence of a hydrophobic Delrin ogive dropped from 50 cm at 5°. The time between images is 15 ms. (b) Axial acceleration measurements. (c) First radial axis acceleration measurements. (d) Second radial axis acceleration measurements. Line *A* corresponds to impact, *B* is pinch-off of the main cavity on the sides of the projectile, *C* is pinch-off of the trailing cavity, and *D* is the time of the final image in the sequence.

3.2 Trajectory & Velocity

The trajectory of each test was computed using the integration procedure outlined in section 2.5.4. A comparison of the findings from the tests for the hydrophilic, hydrophobic, and half-and-half cases will be presented and discussed. The trajectory results will be presented in the form of x and z positions that were obtained by integrating the acceleration data from the IMU twice. The x displacement values are the magnitude from the two radial IMU axes which represent the total lateral displacement of the projectile and are always shown as positive in the trajectory plots even though negative x displacement occurred for some cases. Effectively, all rotation and lateral displacement occurred in the $x - z$ plane with no contribution in the y direction. The mean trajectories for multiple cases (e.g., figure 3.4(a)) were computed by averaging the x displacement for each test at 5-cm intervals along the z axis. The values presented in the velocity plots and tables are ratios of the absolute value of the instantaneous vertical velocity w to the initial vertical impact velocity U_o. All of the positions and velocities are relative to the location of the IMU, which was embedded in the tail of the projectile.

The image sequences in figure 3.2 demonstrate the five main water entry cases used in this study performed for a Delrin ogive. Figure 3.3 shows the trajectories of one drop from each case in table 2.4 plotted with drops from similar cases. The cases shown in 3.3(a) correspond to images sequences 3.2(a) and 3.2(b) depicting vertical ($0°$) water entry for hydrophilic and hydrophobic cases. Figure 3.3(b) relates to image sequence 3.2(c) for half-and-half cases. The angled cases in figures 3.3(c) and 3.3(d) show trajectory plots for image sequences 3.2(d) and 3.2(e), respectively. The trajectory plots of the hydrophilic and hydrophobic $0°$ cases in figure 3.3(a) show that each projectile descends straight down through the water after impact with a peak lateral displacement of 0.55 diameters. The $0°$ case provides the baseline for lateral translation to compare with the half-and-half and oblique entry cases. Figure 3.3(b) shows single drops for the half-and-half cases. For each half-and-half drop, the projectile was aligned such that the hydrophobic half was on the left side relative to the camera. The result was a controlled lateral displacement always to the hydrophilic side with 2 diameters of displacement and approximately 0.85 diameters of variation. Figures 3.3(c) and 3.3(d) show the lateral displacement of $2°$ and $5°$ cases with maxima of 7.7 and 13.2 diameters, respectively.
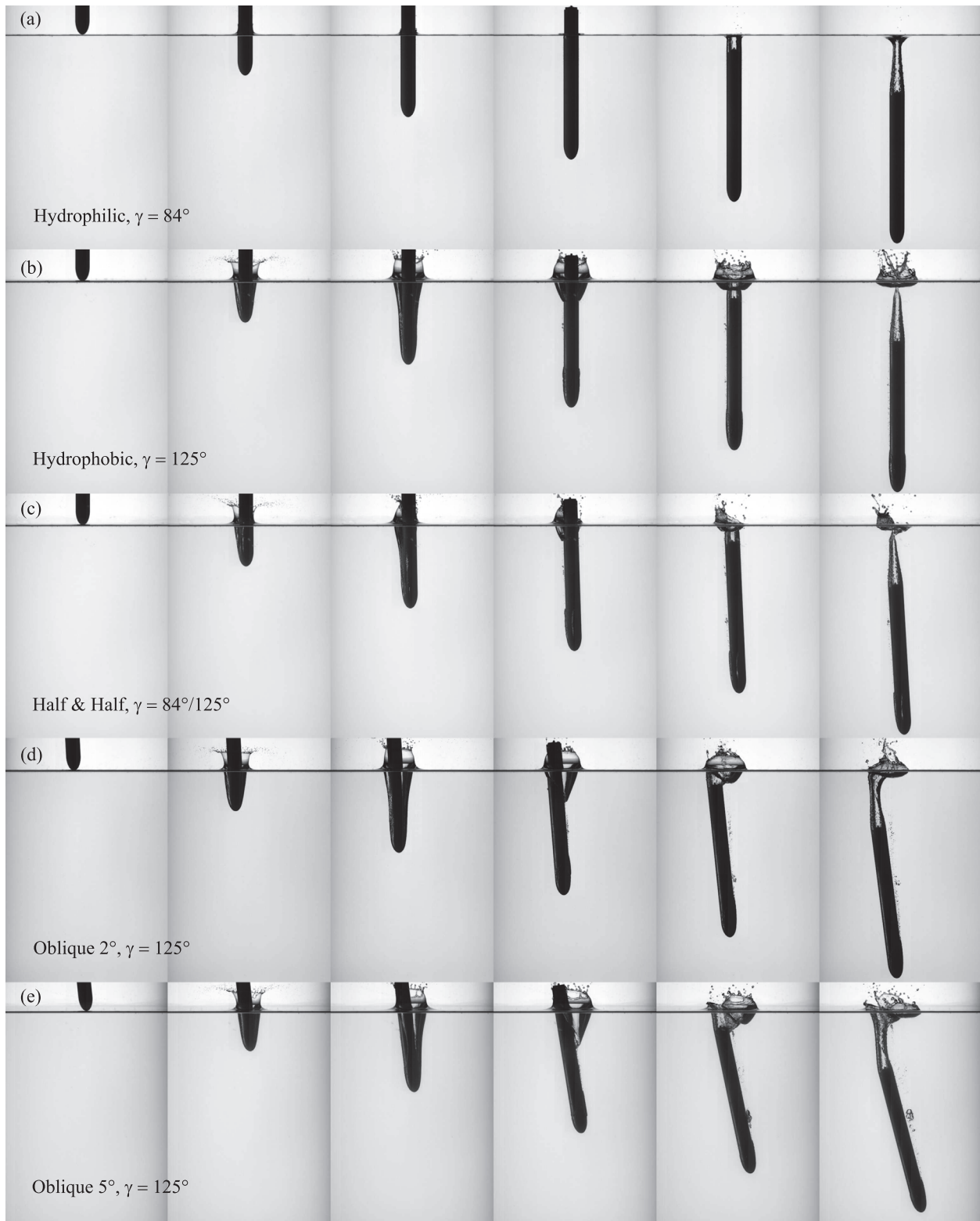
Figure 3.2: Image sequences depicting differences in water entry dynamics of multiple different cases of a projectile with an ogive nose made of Delrin acetal resin. Each projectile was dropped from 50 cm above the surface of the water. The time between each image is 21.1 ms. γ represents the wetting angle of the left and right halves of the projectile, respectively.

(a) Hydrophilic and hydrophobic 0°.

(b) Half & half 0°.

(c) Hydrophobic 2°.
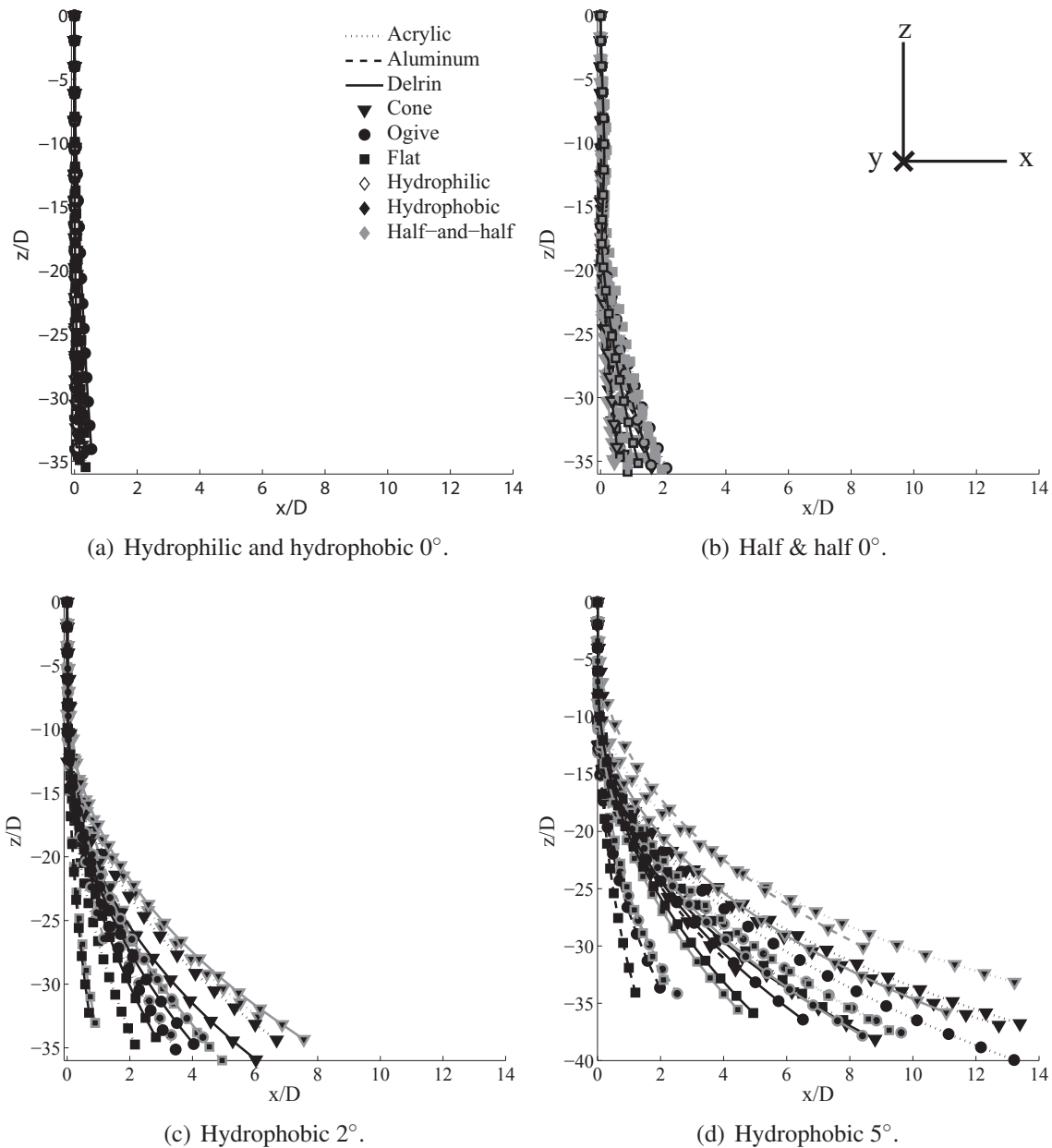
(d) Hydrophobic 5°.

Figure 3.3: (a) Hydrophilic and hydrophobic vertical (0°) entry cases show less than 0.6 diameters of lateral displacement. (b) The half-and-half case resulted in maximum lateral displacement of 2.1 diameters. (c) A 2° impact angle results in a maximum lateral displacement of 7.8 diameters. (d) A maximum lateral displacement of 13.1 diameters is seen for the hydrophobic 5° case. The legend in (a) is used for all for plots. The gray lines represented 36-cm drop heights and the black lines represent 50-cm drop heights. The coordinate frame in (b) is the same for all subsequent trajectory plots. D is the diameter of the projectile (2.54 cm/1 in.). The markers indicate every 50 points.

41

3.2.1 Symmetric Surface Condition, $0°$ Impact Angle

The trajectory curves from figure 3.4 show that minimal (< 0.5 diameter) lateral displacement occurs over 10 tests for both the hydrophobic and hydrophilic cases. Multiple tests were not performed for the other materials and the trajectory characteristics for the $0°$ impact angle are presumed to be similar for all materials. The trajectory of the cone nose shape showed the most variation in the final position and all three nose shapes showed similar variation over the first 20 diameters of descent following impact with the free surface.

The velocities in figure 3.4(g), (e), and (f) were normalized by the impact velocity U_o (3.1 m/s). The w velocity of the projectile continued to increase for 0.0625 s after impact, at which point the deceleration caused by hydrodynamic forces reversed the direction of w, which then decreased at a relatively constant rate, as illustrated in figure 3.5. The peak and final w velocities for each case are presented in table 3.1. The hydrophobic case for both the ogive and flat nose shapes demonstrate a slower final w velocity than for the hydrophilic case. This slower velocity was caused by the momentum transfer from the projectile to the water which was manifest by the splash curtain and cavity. The hydrophobic case for the cone shows a slight increase in velocity compared to the hydrophilic case. Figure 3.6 depicts the differences in splash curtain formation for each nose shape in both the hydrophilic and hydrophobic cases. As seen in figures 3.6(c) and 3.6(f), the nose geometry was responsible for the splash curtain that forms for the cone hydrophilic case and is due to the sharp corner transition at the base of the nose. The minimal difference between the hydrophilic and hydrophobic cone velocity values was due to the formation of a cavity in both cases.

Truscott et al. [3] showed that hydrophobic spheres had increased velocity compared to hydrophilic. This difference between spheres and slender axisymmetric bodies could be due to the long body inhibiting vortex shedding in both hydrophilic and hydrophobic cases as well as the increased hydrodynamic drag for the hydrophobic case. Further study of the slender axisymmetric bodies using PIV would be beneficial to understand the what causes the velocity differences.

(a) Cone trajectory.　　　　(b) Ogive trajectory.　　　　(c) Flat trajectory.

(d) Cone *w* velocity.　　　　(e) Ogive *w* velocity.　　　　(f) Flat *w* velocity.

(g) Cone *v* velocity.　　　　(h) Ogive *v* velocity.　　　　(i) Flat *v* velocity.
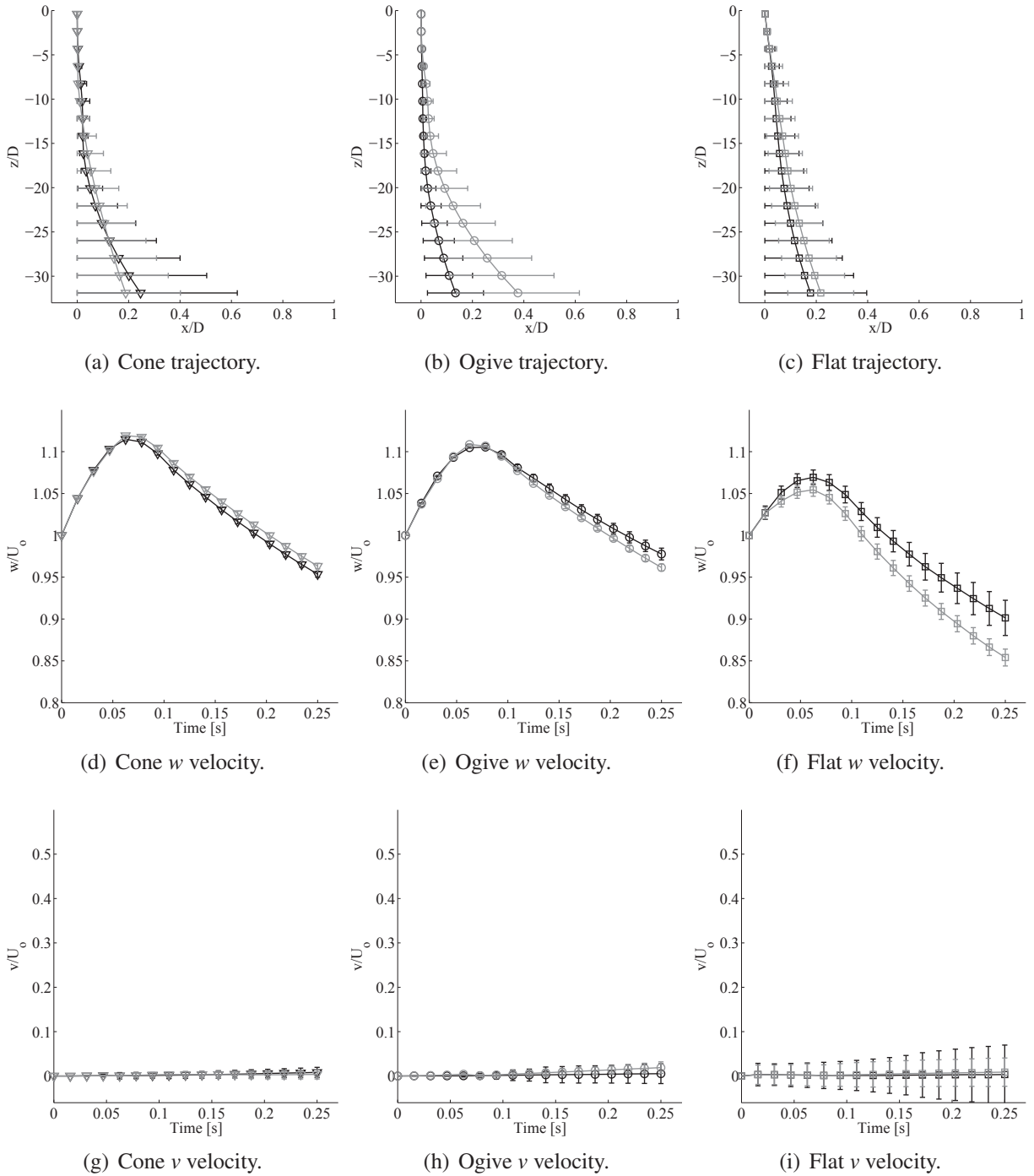
Figure 3.4: Mean trajectories (top row) and mean z velocities (bottom row) for 10 tests each of $0°$ hydrophilic (dark) and $0°$ hydrophobic (light) cases for cone, ogive, and flat nose shapes are plotted with a 95% confidence interval. The trajectory plots are normalized by the projectile diameter D in both the x and z directions. The velocity plots are normalized by the vertical impact velocity U_o in z. Markers represent 5-cm increments in z for the trajectory plots and every 50 data points for the velocity plots.

43
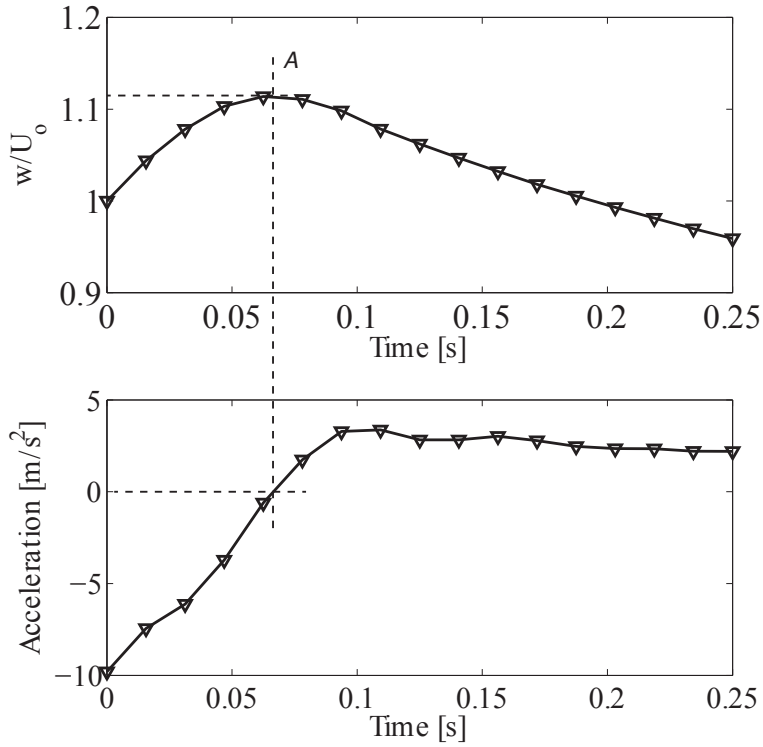
Figure 3.5: The instantaneous vertical velocity w and z-direction acceleration are compared. A shows that the reversal in w occurs immediately after the acceleration passed 0 m/s^2.

Table 3.1: Final x position and peak and final w velocities for all three nose shapes at $0°$ inclination shown in figure 3.4. The hydrophobic cone achieves the highest peak velocity at 1.12 and the hydrophobic flat experiences the largest decrease in velocity, ending at 0.85.

Nose Shape	Case	Final x	Peak w	Final w
Cone	Hydrophilic	0.25	1.11	0.95
	Hydrophobic	0.19	1.12	0.96
Ogive	Hydrophilic	0.13	1.10	0.97
	Hydrophobic	0.38	1.11	0.96
Flat	Hydrophilic	0.18	1.07	0.90
	Hydrophobic	0.22	1.05	0.85
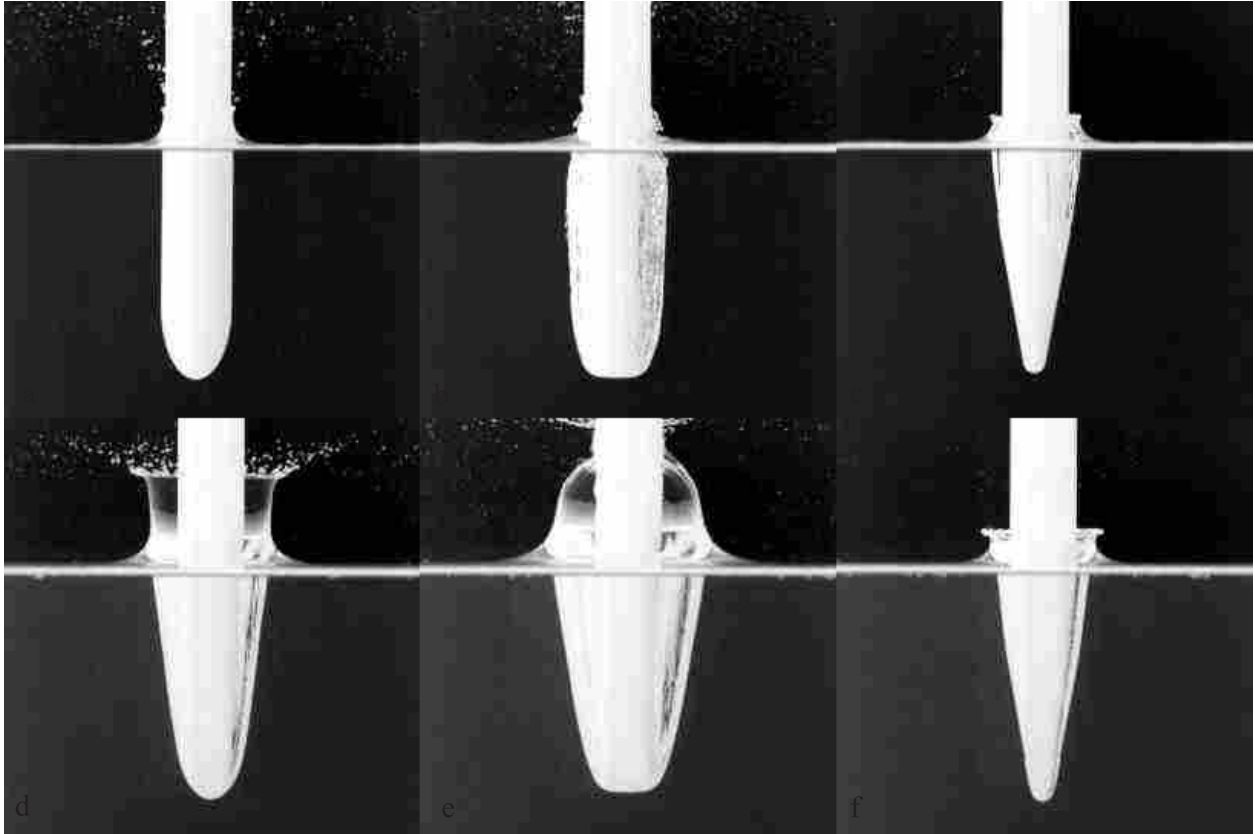
Figure 3.6: Images of difference splash curtains for Delrin projectiles. The top row is hydrophilic and the bottom row is hydrophobic. The nose shapes from left to right are ogive, flat, and cone. Each image was taken 25 ms after impact.

3.2.2 Symmetric Surface Condition, Oblique 5° Impact Angle

The initial impact angle significantly affects the rotation and lateral translation of the projectile. The plots in figure 3.7 present the mean trajectories and velocities for 10 repeated cases of hydrophilic and hydrophobic cones, ogive, and flat noses. Figure 3.7(a) shows that both the hydrophilic and hydrophobic cone cases experiences 7 diameters of displacement. The hydrophilic ogive case presented in figure 3.7(b) shows 7 diameters of displacement and the hydrophobic case shows a displacement of 5 diameters. The flat nose in figure 3.7(c) experiences 6.5 diameters for the hydrophilic case and 4 diameters of displacement for the hydrophobic case. The cone also has much more variation in the final lateral position than either the flat or the ogive noses, which is partially a result of the increased IMU error over longer distances traveled. The cone nose shape is responsible for the greater lateral displacement. Comparing the trajectories from figure 3.4 with

45

Table 3.2: Final x position and peak and final w velocities for all three nose shapes of the hydrophobic 5° case. The cone and ogive achieved peak velocities at 1.10 and the cone experiences the largest decrease in velocity, ending at 0.71.

Nose Shape	Case	Final x	Peak w	Final w
Cone	Hydrophilic 5°	8.25	1.11	0.71
	Hydrophobic 5°	8.13	1.10	0.71
Ogive	Hydrophilic 5°	6.94	1.11	0.78
	Hydrophobic 5°	4.85	1.10	0.84
Flat	Hydrophilic 5°	6.64	1.10	0.77
	Hydrophobic 5°	3.64	1.05	0.78

figure 3.7 reveals the large effect both a slight angle and different nose shape have on the movement of slender projectiles during water entry.

The peak and final velocities for the oblique 5° case are shown in table 3.2. It is interesting to note that the final z-direction velocity of the cone was less than that of the flat. This was due to rotation of the projectile which increased vertical drag and the horizontal side force of the cone more than the flat nose (see sections 3.3.3 and 3.3.4). Comparing the velocities of the oblique entry to the vertical entry shows a significant (> 0.1) decrease in final velocity for all cases, but only a slight (≈ 0.01) decrease in peak velocity.

3.2.3   Asymmetric Surface Condition (Half-and-Half), 0° Impact Angle

The initial impact of the projectiles with a hydrophobic coating on one half produces an asymmetric splash curtain (see figure 3.8). The momentum imbalance resulting from the asymmetry causes the nose of the projectile to move toward the hydrophilic side of the projectile. Once the projectile is no longer aligned vertically, a moment couple between gravity, acting through the center of mass, and the center of pressure, applied toward the nose of the projectile, causes the projectile to rotate in a counter-clockwise fashion. The projectile experiences both continued rotation and a lateral translation toward the hydrophilic side. Figure 3.9 presents the trajectories and velocities for 10 averaged half-and-half tests performed for the cone, ogive, and flat. Comparing figure 3.9(c) to figures 3.9(a) and 3.9(b) shows that the projectiles with the flat nose shape undergo a larger lateral translation than the projectiles with the cone or ogive nose shapes due to the larger

(a) Cone trajectory.   (b) Ogive trajectory.   (c) Flat trajectory.

(d) Cone w velocity.   (e) Ogive w velocity.   (f) Flat w velocity.

(g) Cone v velocity.   (h) Ogive v velocity.   (i) Flat v velocity.
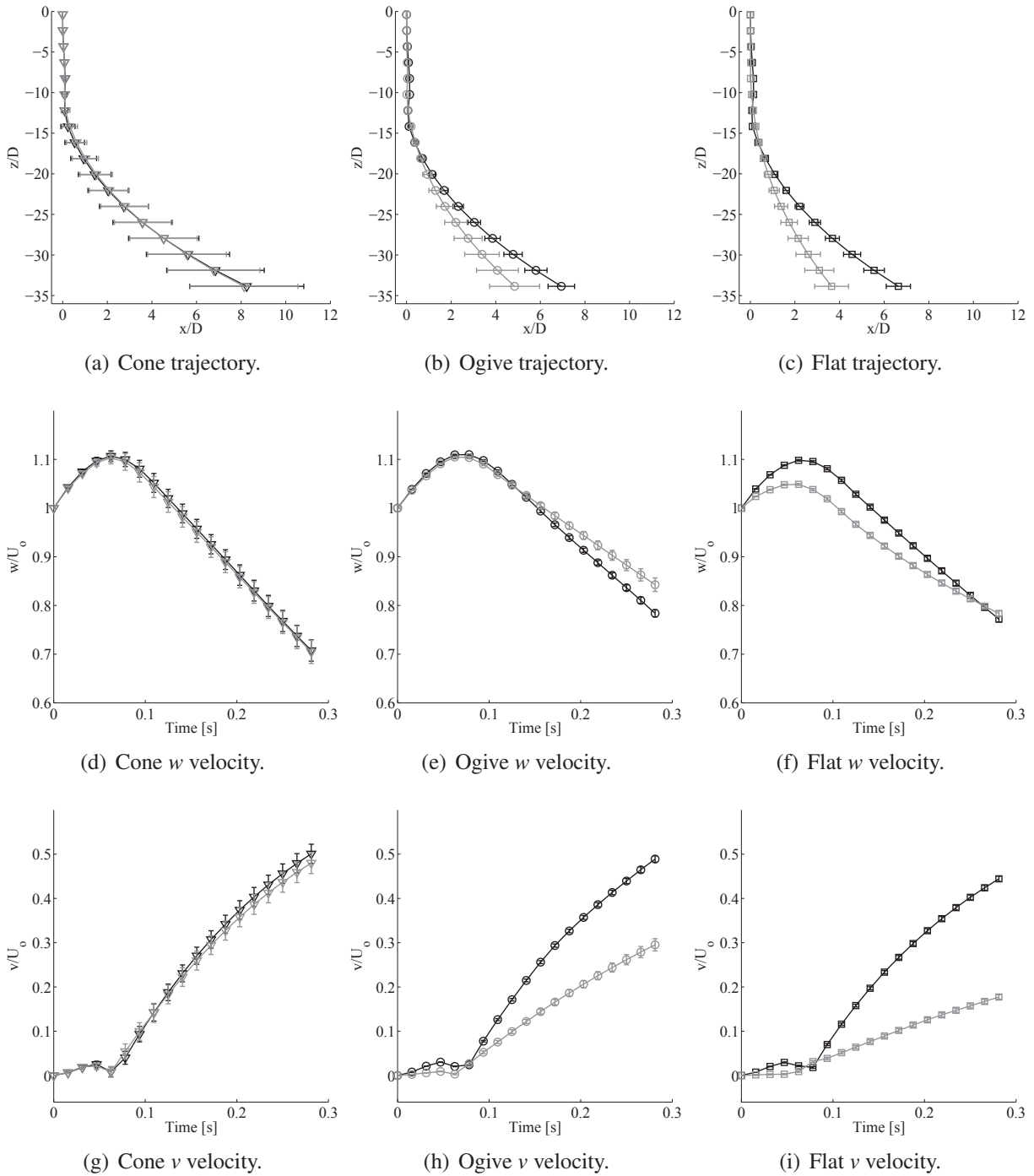
Figure 3.7: Mean trajectories (top row), mean vertical velocities (middle row), and mean lateral velocities (bottom row) for 10 of each of the hydrophilic (black) $5°$ and hydrophobic (gray) $5°$ cases for cone, ogive, and flat nose shapes are plotted with a 95% confidence interval. The trajectory plots are normalized by the projectile diameter D in both the x and z directions and the velocity plots are normalized by the impact velocity U_o. Markers represent 5-cm increments in z for the trajectory plots and every 50 data points for the velocity plots.

47

Table 3.3: Final *x* position and peak and final *w* velocities for all three nose shapes of the half-and-half case. The cone achieves the highest peak *w* velocity at 1.12 and the flat experiences the largest decrease in *w* velocity, ending at 0.85.

Nose Shape	Case	Final *x*	Peak *w*	Final *w*
Cone	Half-and-half	0.52	1.12	0.95
Ogive	Half-and-half	0.77	1.11	0.95
Flat	Half-and-half	1.23	1.06	0.85

momentum transfer on the hydrophobic side as is shown in figure 3.8 by a larger splash curtain. The protruding region *A* in figure 3.9(c) demonstrates the displacement of the IMU that is located in the tail of the projectile instead of the nose. As the nose is moved to the right (positive *x*) and the projectile rotates counter-clockwise, the tail moves to the left (negative *x*). As the projectile continues to descend, the position of the IMU crosses the centerline into the positive *x* region. Since the magnitude of the lateral displacement is plotted, all of the values appear positive. A similar protruding region occurred for the oblique angle cases, but was much smaller and not noticeable on the plots.

The peak and final *w* velocities are given in table 3.3. The final *w* velocities of the cone and ogive are higher for the half-and-half case than for the oblique 5° case from section 3.2.2 because the projectiles were initially aligned vertically and did not experience as much rotation as they did in the oblique 5° case. The final velocities for the cone half-and-half case show no change compared to the hydrophilic 0° case and a decrease of 0.01 compared to the hydrophobic 0° case. The final velocities for the flat nose do not change for the hydrophobic and half-and-half cases, but the final vertical velocity deceases from 0.9 to 0.85 when comparing the hydrophilic and half-and-half cases. The ogive nose shape results in a slight decrease of 0.01 from hydrophobic to half-and-half, and a decrease of 0.97 to 0.95 going from hydrophilic to half-and-half. The decrease in the vertical velocity for between the 0° entry cases and the half-and-half case is due to the rotation of the projectile in the half-and-half case which results in more vertical drag. The peak *w* velocities for the cone and ogive half-and-half case are the same as the hydrophobic 0° case, and the flat half-and-half case *w* velocity increase from 1.05 to 1.06 when compared to the hydrophobic 0° case.
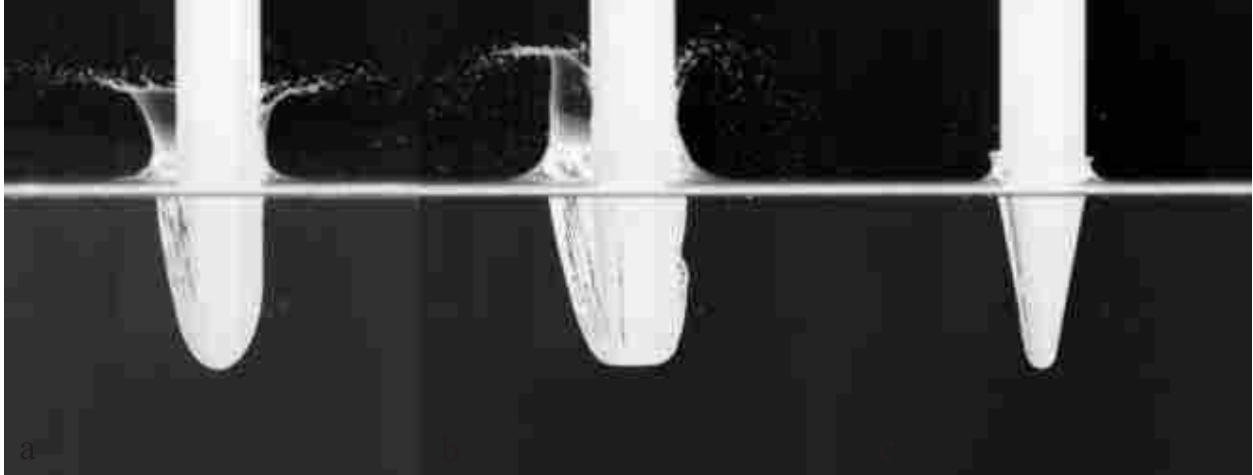
Figure 3.8: Images of difference splash curtains for Delrin projectiles for half-and-half cases. The left half of each projectile is coated with a hydrophobic spray and the ride half is hydrophilic. Obvious splash curtain and cavity asymmetry are seen in (a) and (b), with only a minor asymmetry in (c). The images are taken 15 ms after impact.

3.2.4   Center of Mass Effects

A series of tests were performed to validate the theory of a moment couple between the center of gravity and the center of pressure being responsible for the rotation and lateral displacement discussed in the previous sections. The location of the center of mass was varied and the effect was observed both for an angled hydrophobic case as well as for a half-and-half case for a modified Delrin ogive dropped from 50 cm. Figure 3.10 qualitatively demonstrates the effect of moving the center of mass a distance d from close to the nose (d=8.63 cm, *close*), to approximately the middle of the projectile (d=12.63 cm, *middle*), and to approximately halfway between the nose and the middle (d=10.63 cm, *half*) of the projectile. The center of mass for the *middle* case was similar to the center of mass for the original Delrin ogive of 12.5 cm. A similar location was chosen due to the change in relative density with the inclusion of the lead slug. It is clear from the images in the final column in figure 3.10 that the amount of rotation increases as the location of the center of mass is moved farther from the nose and the reason for this will be discussed in section 3.3.2.

Figure 3.12 presents the trajectories and velocities for three locations of the center of mass tests. The effect of moving the center of mass along the axis of the projectile is clear from the differences in lateral displacement for the hydrophobic 50-cm case shown in figure 3.11 and the half-and-half 50-cm case shown in figure 3.12. Figure 3.11(c) presents the case with the center

(a) Cone trajectory.

(b) Ogive trajectory.

(c) Flat trajectory.

(d) Cone *w* velocity.

(e) Ogive *w* velocity.

(f) Flat *w* velocity.

(g) Cone *v* velocity.

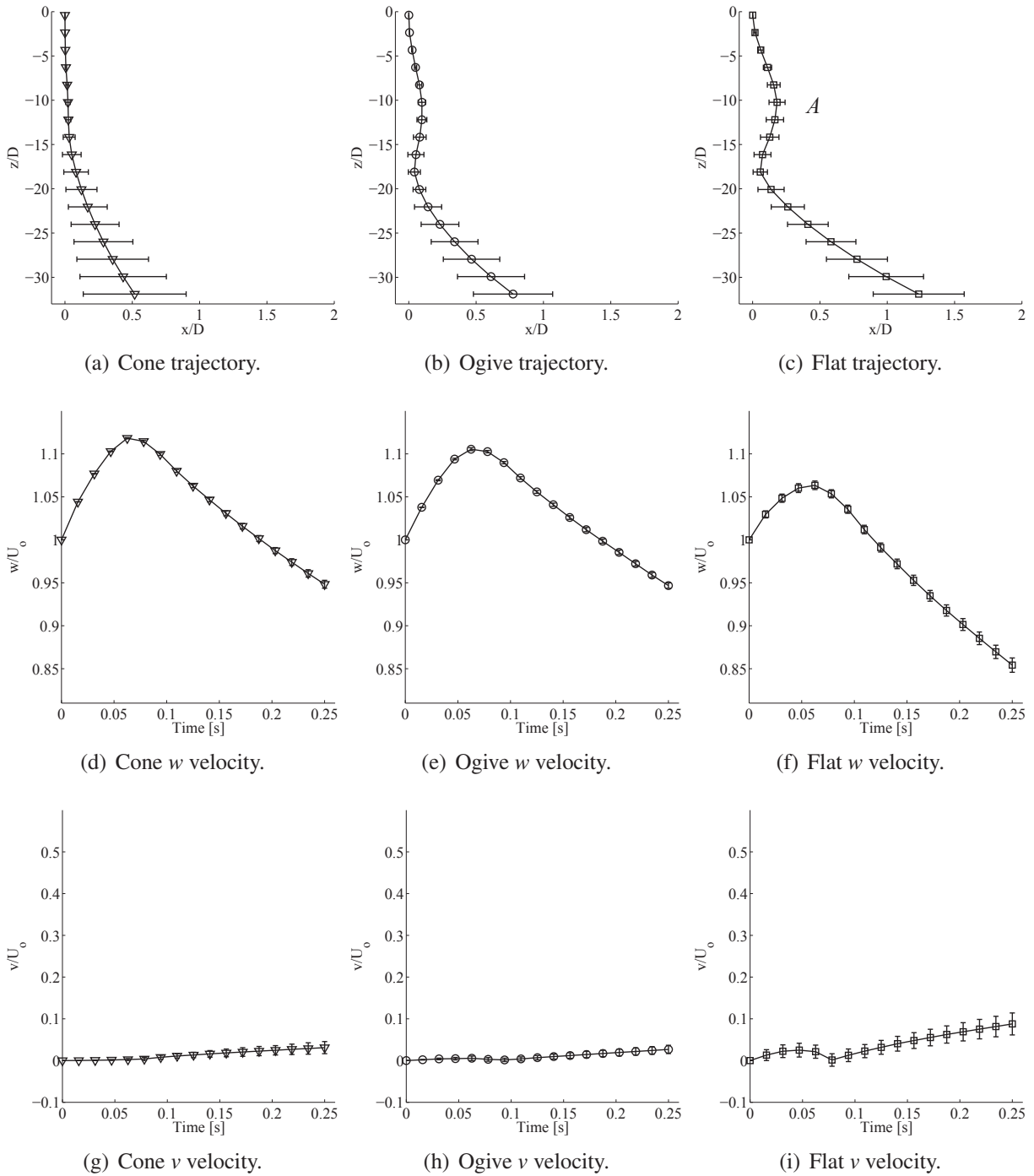(h) Ogive *v* velocity.

(i) Flat *v* velocity.

Figure 3.9: Mean trajectories (top row) and mean vertical velocities (bottom row) for 10 tests each of the half-and-half case for cone, ogive, and flat nose shapes are plotted with a 95% confidence interval. The trajectory plots are normalized by the projectile diameter D in both the horizontal and vertical directions. The velocity plots are normalized by the vertical impact velocity U_o in z and represent the ratio of the instantaneous velocity to the impact velocity.

Table 3.4: The peak and final w velocities for a modified hydrophobic Delrin ogive for the 5°
case. All three locations for the center of mass achieve a peak velocity of approximately
1.13 and the case with the center of mass farthest from the nose experiences
the largest decrease in velocity, ending at the impact velocity.

Case	Final x	d	Peak w	Final w
Hydrophobic 5°	3.78	12.63 cm	1.13	1.05
Hydrophobic 5°	3.21	10.63 cm	1.13	1.08
Hydrophobic 5°	2.38	8.63 cm	1.13	1.12
Half-and-half	1.69	12.63 cm	1.13	1.09
Half-and-half	1.19	10.63 cm	1.13	1.12
Half-and-half	0.66	8.63 cm	1.14	1.14

of mass closest to the nose which shows the least lateral displacement at 2.1 diameters. A lateral displacement of 3.9 diameters is observed when the center of mass is farther from the nose in figure 3.11(a). The velocities for all three cases are shown in table 3.4. All three cases reach the same peak velocity at 1.13. The *middle* case has the largest decrease in vertical velocity, ending at 1.05 due to the greater rotation and lateral displacement of this case. The velocity profiles for these center of mass cases have a different from than the velocity plots seen in previous sections due to the additional mass from the lead slug. The lead slug is extremely close to the nose for the tests presented in figure 3.11(i) and between the minimal relative rotation and the added mass there is very little deceleration after the projectile reaches peak velocity. Similar effects are seen in figures 3.11(g) and 3.11(h) with the final velocity remaining above impact velocity.

Changing the location of the center of mass also affects the half-and-half case as shown in figure 3.12. The regular half-and-half ogive case from section 3.2.3 had a peak lateral displacement of 0.7 diameters. Moving the center of mass to the *half* and *middle* locations increases the amount of lateral displacement to 1.19 and 1.69 diameters, respectively. The 8.63-cm case results in a slightly decreased displacement of 0.65 diameters.

3.2.5   Non-dimensional Pinch-off Time

The occurrence of two pinch-off events was mentioned in section 1.1 and a discussion of the non-dimensional time to each pinch-off event follows. Figure 3.13(b) presents the non-dimensional time to pinch-off that occurs on the sides of the projectile (figure 1.1(f); gray markers)

Figure 3.10: Image sequences of a modified hydrophobic Delrin ogive dropped from 50 cm with the center of mass located at 12.63 cm, 10.63 cm, and 8.63 cm from the nose of the projectile. The time between each image is 32.0 ms and the impact velocity was 3.1 m/s.

and pinch-off of the trailing cavity (figure 1.1(g); black markers) for 10 tests of each Delrin nose shape. The time t is normalized by the impact velocity U_o and projectile diameter D. Pinch-off on the side of the projectile did not occur for the hydrophilic cases, so only show black markers are shown for these cases.

The on-body pinch-off data show good grouping of the flat nose shapes around $t^* = 8$, with less pronounced grouping of the ogive and cone nose shapes close to $t^* = 6$. The greater t^* value for the flat nose indicates that the subsurface cavity collapses slower than for the cone and ogive nose shapes. Data for pinch-off of the trailing cavity show a slight grouping trend with the flat, ogive, and cone noses in decreasing order. As expected, all of the t^* values for pinch-off of the

(a) Trajectory for d = 12.63 cm.

(b) Trajectory for d = 10.63 cm.

(c) Trajectory for d = 8.63 cm

(d) Velocity for d = 12.63 cm.

(e) Velocity for d = 10.63 cm.

(f) Velocity for d = 8.63 cm.

(g) Velocity for d = 12.63 cm.

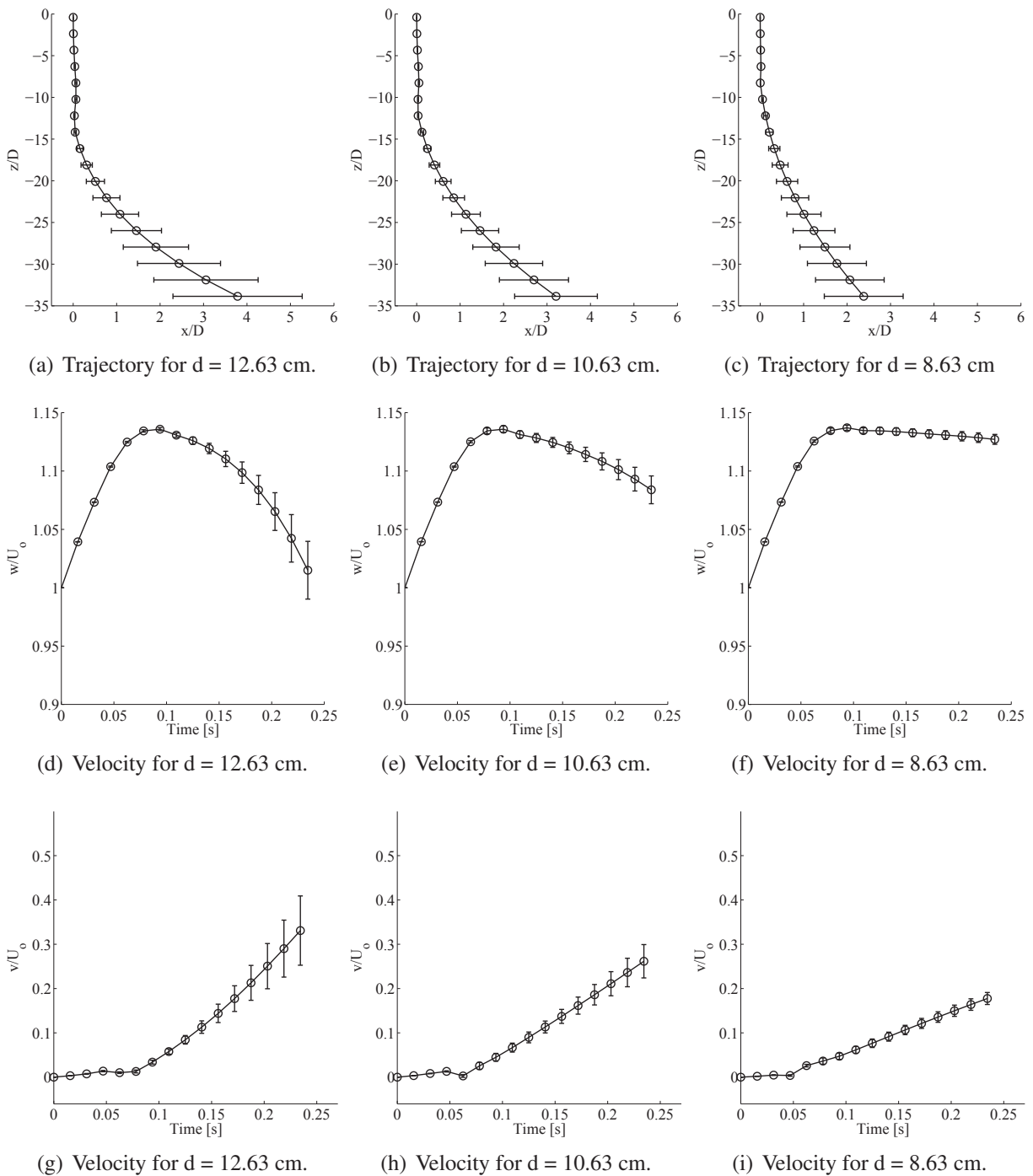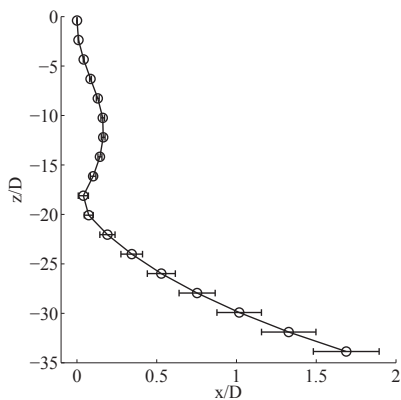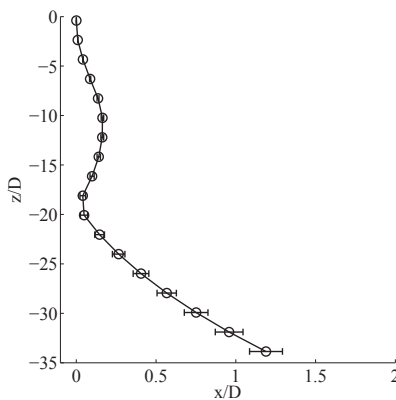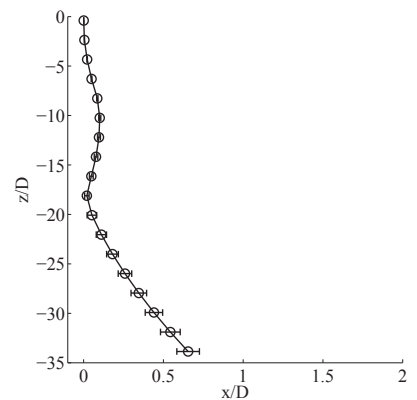(h) Velocity for d = 10.63 cm.

(i) Velocity for d = 8.63 cm.

Figure 3.11: A hydrophobic projectile with an ogive nose shape made of Delrin was dropped from 50 cm at a 5° impact angle. A lead slug of mass 102.1 gm was used to change the location of the center of mass of the projectile. Three different center of mass locations were used, measuring (a) 12.63 cm, (b) 10.63 cm, and (c) 8.63 cm from the nose of the projectile.

(a) Trajectory for d = 12.63 cm.　　(b) Trajectory for d = 10.63 cm.　　(c) Trajectory for d = 8.63 cm

(d) Velocity for d = 12.63 cm.　　(e) Velocity for d = 10.63 cm.　　(f) Velocity for d = 8.63 cm.
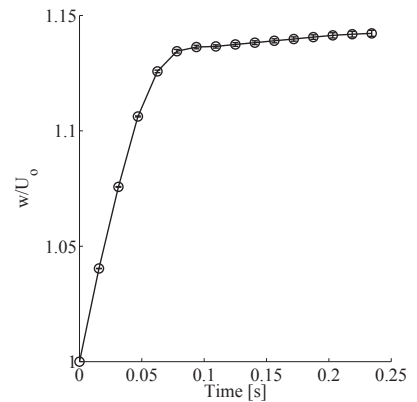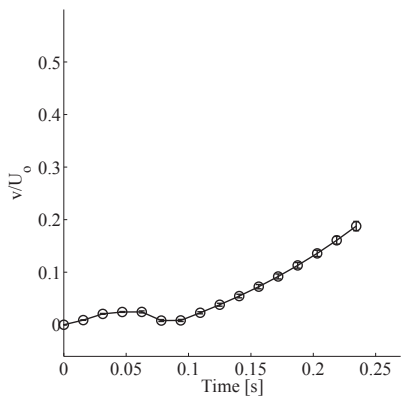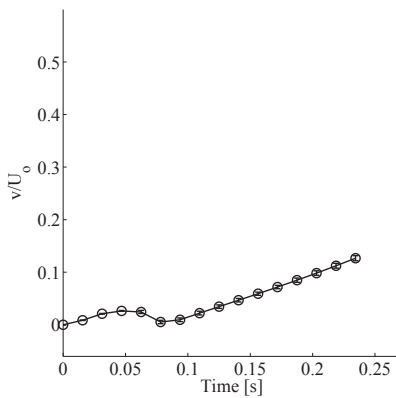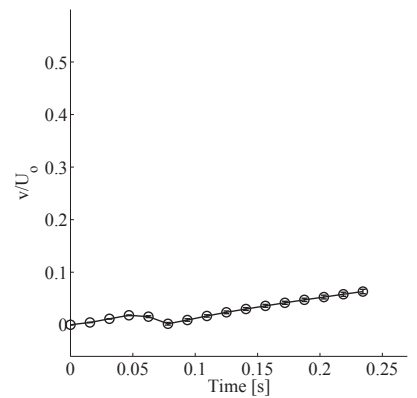
(g) Velocity for d = 12.63 cm.　　(h) Velocity for d = 10.63 cm.　　(i) Velocity for d = 8.63 cm.

Figure 3.12: A half-and-half coated projectile with an ogive nose shape made of Delrin was dropped from 50 cm. A 102.1 gm lead slug was used to change the location of the center of mass of the projectile. Three different center of mass locations were used, measuring (a) 12.63 cm, (b) 10.63 cm, and (c) 8.63 cm from the nose of the projectile.
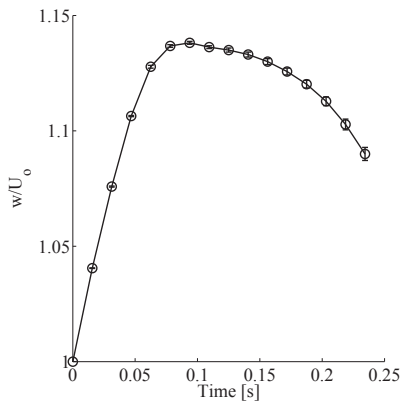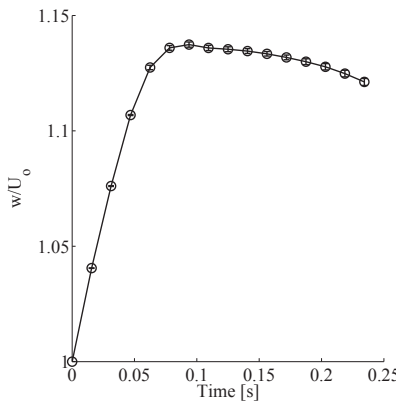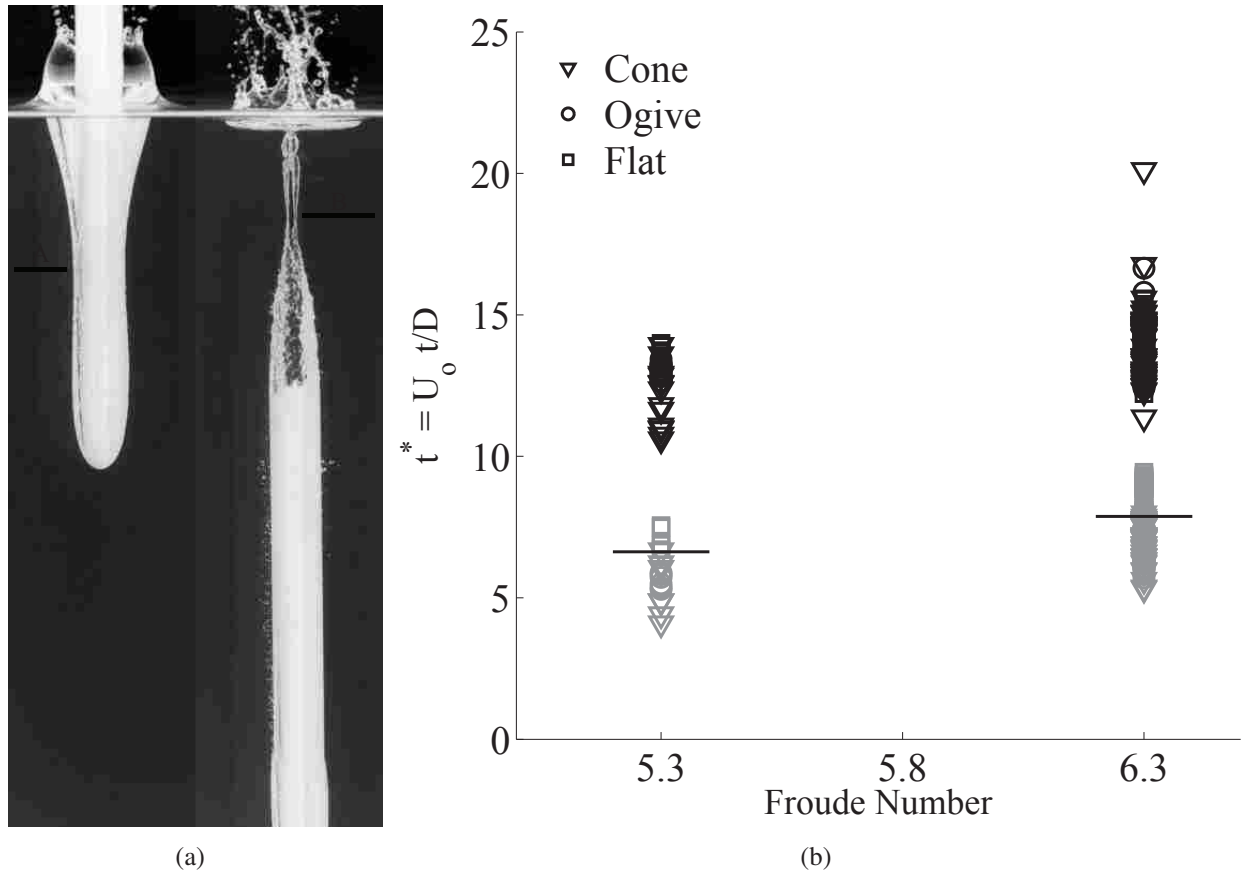
Figure 3.13: (a) Pinch-off location on the side of the projectile (A) and of the trailing cavity (B). (b) Non-dimensional pinch-off time t^* for 10 tests of each Delrin nose shape and case. The gray markers are for hydrophobic cases in which pinch-off occurred on the sides of the projectile (figure 1.1(f)). The black markers represent pinch-off of the trailing cavity (figure 1.1(g)). The horizontal at $t^* = 7.875$ represents the predicted t^* value for spheres from Truscott et al. [35]

trailing cavity occur after the on-body pinch-off values. These findings demonstrate that the nose shape has a minor effect on the time to pinch-off on the sides of the projectile.

The data presented in figure 3.13(b) were compared with the non-dimensional pinch-off times calculated by Truscott et al. [35] for spheres. The calculated t^* for the slender axisymmetric projectiles, especially the flat nose, generally follow the trend presented by by Truscott et al. for a Froude number of 6.3, and is shown as a horizontal line in figure 3.13(b). The deviation from the predicted values for the ogive and cone can likely be attributed to the differences in geometry and the oblique entry angle.

3.3 Effect of Forces on Water Entry

This section discusses the effect of forces on the projectile during the water entry event. The impact forces will be discussed first, followed by a discussion the drag coefficients and lift coefficients.

3.3.1 Impact Forces

The principal forces of interest occur at impact. Understanding how nose shape and wetting angle affect the impact force will enable engineers to design the nose geometry to mitigate potential destructive impact forces. Figure 3.14 presents the peak impulsive force experienced by each nose shape for four impact cases. Each force shown represents the magnitude of all three accelerometer axes calculated by

$$F_{mag} = m_p \sqrt{a_x^2 + a_y^2 + a_z^2}, \qquad (3.1)$$

where m_p is the mass of the projectile and a_i is the accelerometer axis.

The calculated forces experienced by the projectile in each test are presented in figure 3.14. The projectiles with the flat nose shape experienced 10 times more impact force than projectiles with either the cone or the ogive nose shapes due to the blunt flat geometry. The flat nose impact force values for the hydrophilic, hydrophobic, and half-and-half cases include axial forces that exceed the measurable limit of the accelerometer (± 16 g), so the measured values are the maximum measurable value. An accelerometer capable of measuring accelerations greater than ± 16 g was not available in a size for use in the embedded design used in this study. The impact force experienced by the flat nose shape can be significantly reduced by angling the projectile, as shown in the *Phobic 5°* column of figure 3.14(a). Changing the impact angle for the flat from 0° to 5° eliminates the impact directly on the blunt portion of the nose and decreases the overall force experienced by the flat projectile. Changing the angle for the cone and ogive does not result in an appreciable change in the impact force, as shown in figure 3.14(b). Figure 3.14(b) does show that the cone nose shape experiences little more than a 1 N maximum impact force and the ogive experiences an impact force of up to 2.5 N. The findings from figures 3.14(a) and 3.14(b) demonstrate that varying the wetting angle has no effect on the total impact force, but angling the flat nose shape will decrease the impulsive force on impact.
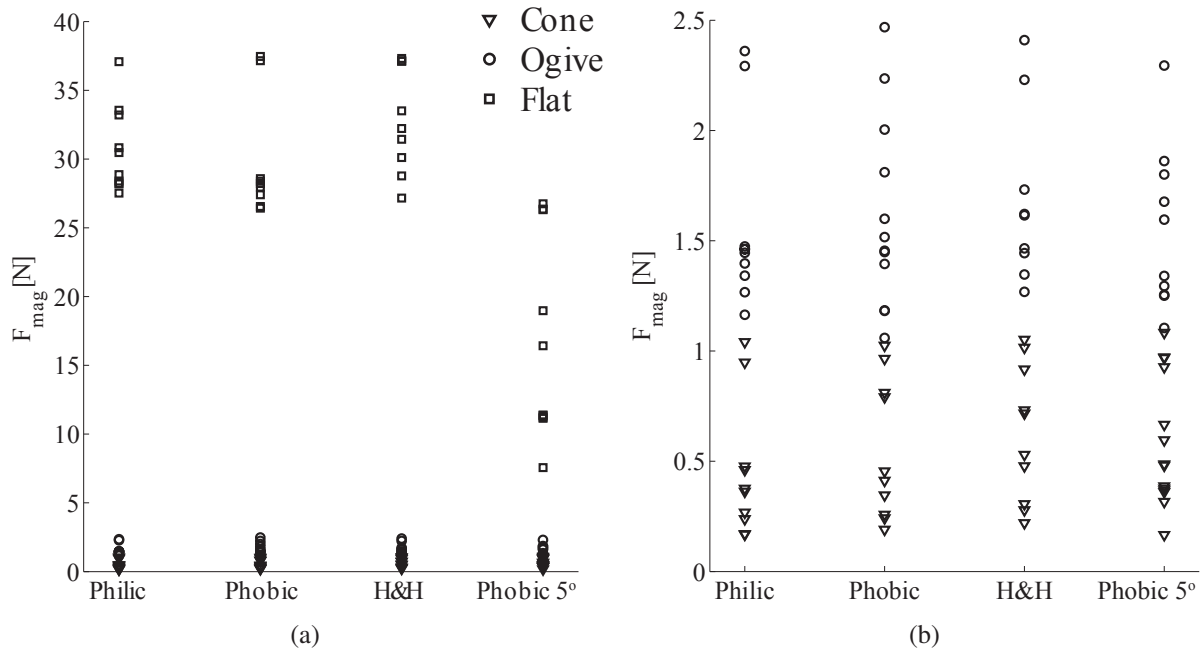
Figure 3.14: (a) Maximum force F_{mag} experienced by Delrin projectiles at impact for 10 tests each of various cases shown on the horizontal axis. (b) Detail view of figure (a) without the flat cases.

The large distribution of the presented force values is partially an aliasing artifact of the digital sampling process from the accelerometer. The capacitors attached to the microbeams (section 2.5.1) produce an analog signal proportional to acceleration that is sampled at 3200 Hz. The impact duration can be as short as 0.6 ms (two samples) and as long as 1.88 ms (six samples) when sampling values exceeding the maximum measurable limit. The actual peak force could potentially occur between samples, thus showing lower forces than what actually occurred. The aliasing problem could be reduced by using an accelerometer capable of a faster sampling rate, but this was not feasible for this study.

3.3.2 Center of Pressure

A projectile entering the water at an oblique angle will experience a moment couple from gravity acting through the center of mass and from the center of pressure acting toward the nose of the projectile. If the center of gravity is farther from the nose than the center of pressure, the projectile will be rotationally unstable. The concept of rotational instability of a floating or
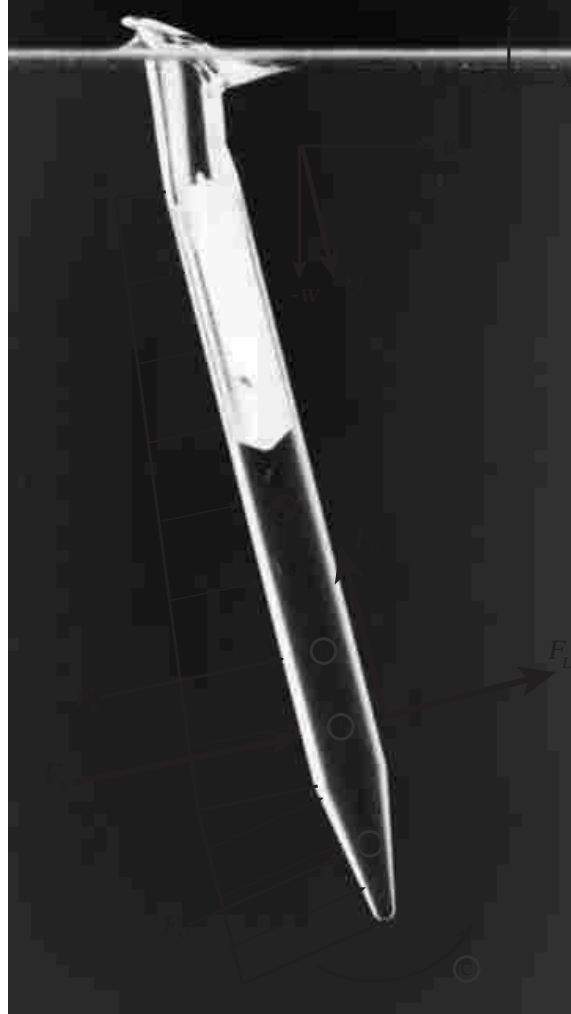
Figure 3.15: N and B represent the locations of the center of pressure on the nose and projectile, respectively. T is the total center of pressure for the projectile. The forces F_N, F_B, and F_T are the resultant forces acting at N, B, and T, respectively. U is the total velocity of the projectile. A moment couple between gravity g and F_T cause the projectile to rotate in the direction of C.

submerged body is well known and will be discussed briefly inasmuch as it relates to the rotation of the projectiles herein.

The center of pressure is the point at which the resultant force from the fluid acts on a submerged portion of a body. The resultant force acts normal to the body at the center of pressure and is the product of the surface area of the body and pressure at the centroid of the body [28]. In this study, the resultant force is the hydrodynamic force F_T. Furthermore, F_T can be resolved into drag and lift forces, F_D and F_L, and their effects will be discussed in sections 3.3.3 and 3.3.4.

Figure 3.15 illustrates the placement of key forces relevant to the lateral displacement of slender projectiles in the water. The point T represents the total center of pressure of the body at an instant in time. Point B is the center of pressure of just the body and point N is the center of pressure for the nose section of the projectile. The center of pressure N, at the nose, plays an important role in the rotation and lateral displacement of the projectiles and changes based on nose geometry. The angle of the resultant force F_N on the long, angled surface of the cone produces a larger force component in the $+z$ direction, which increases the magnitude of the moment couple and results in more rotation and lateral displacement. Likewise, the ogive would be expected to have more lateral displacement than the flat and comparing figures 3.7(b) and 3.7(c) shows that this is indeed true.

3.3.3 Drag Coefficients

Instantaneous drag coefficients for each projectile case were calculated by

$$C_D = \frac{2F_D}{\rho U^2 A} \tag{3.2a}$$

$$F_D = m_p a_D, \tag{3.2b}$$

where F_D is the drag force, m_p is the mass of the projectile, a_D is the measured acceleration in the relative direction of the fluid, ρ is the density of the projectile, v is the velocity of the projectile, and A is the frontal area of the projectile (5.0671e-4 m^2, for 1-inch diameter). Figure 3.16(a) presents the instantaneous drag coefficient of a hydrophilic cone through time overlaid with a polynomial fit line, which is similar averaged drag coefficients in the other three plots. The data were filtered using the same 50 Hz low-pass Butterworth filter described in section 2.5.5. The drag coefficient increases at constant rate until $t = 0.0947$ s, at which time the cavity pinch-off occurs and a ripple phenomenon is observed on the sides of the bubble cavity (see section 3.4.1). A third-degree polynomial fit line was calculated and the drag coefficient was obtained for each time step to show the general trend without the oscillation in the data. A polynomial fit was not used for the averaged cases.

Table 3.5: Final drag coefficient values used to calculate the terminal velocities.
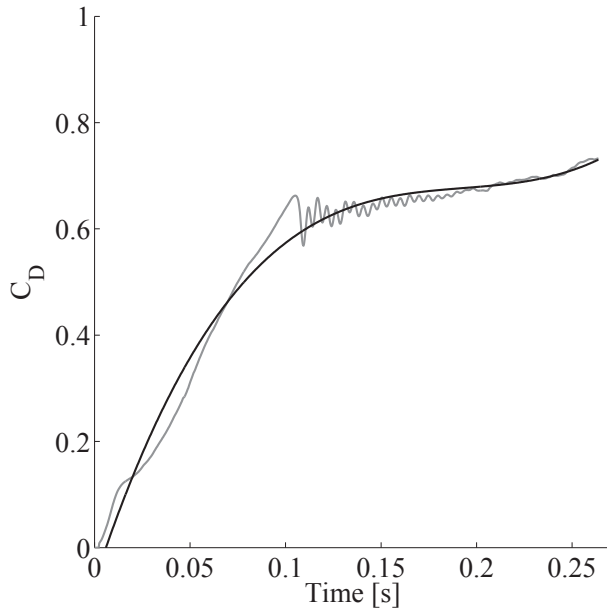
Nose	Hydrophilic 0°	Hydrophilic 0°	Half-and-half	Hydrophilic 5°	Hydrophobic 5°
Cone	0.73	0.73	0.74	0.75	0.79
Ogive	0.66	0.69	0.72	0.64	0.70
Flat	0.77	0.89	0.90	0.70	0.91

Figure 3.16(b) shows that the drag coefficients for the ogive and flat nose shapes are larger for the hydrophobic case, but the drag coefficients for the cone shape for both hydrophobic and hydrophilic cases are almost identical. The increased drag for the hydrophobic cases indicates that the formation of the cavity subjects the projectile to higher forces than the hydrophilic case. For the cone, a cavity was seen to open even for the hydrophilic case in figure 3.6 and this is the cause for the nearly identical drag coefficients. Figure 3.16(c) shows drag coefficient results for the half-and-half case for the cone, ogive, and flat nose shapes that are very similar to the hydrophilic drag coefficients in figure 3.16(b). The similarity is is due to the half-and-half cases undergoing only a little more rotation than the hydrophilic and hydrophobic 0° case. Figure 3.16(d) shows a decrease in drag coefficient because more of the resultant force is contributing to lift, as will be shown in section 3.3.4. For all cases, the flat nose produced the largest drag coefficient due to the blunt nose geometry and the cone and ogive are similar in the amount of drag produced by the nose geometry.

Terminal velocities for each case were computed using

$$U_t = \sqrt{\frac{2(W - F_b)}{C_D \rho A}}, \tag{3.3}$$

where W is the weight of the projectile, F_b is the buoyant force acting on the projectile, C_D is the drag coefficient, ρ is the density of the water, and A is the frontal area of the projectile. The final drag coefficient value for each nose and surface coating and are presented in table 3.5 and were used to calculate the terminal velocities in equation 3.3. The terminal velocities values are presented in table 3.6 and represent a fraction of the impact velocity. The effect of projectile rotation was included in C_D. The ogive nose shape produced a higher terminal velocity for all cases, which would be expected because the final drag coefficient values were the lowest for each case.
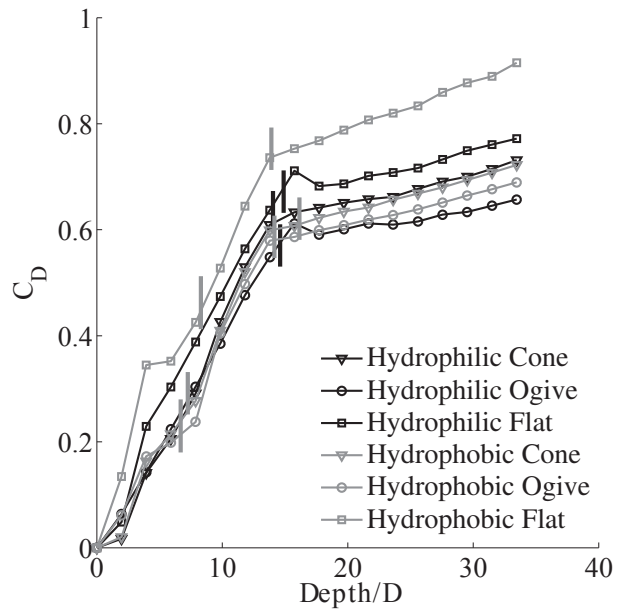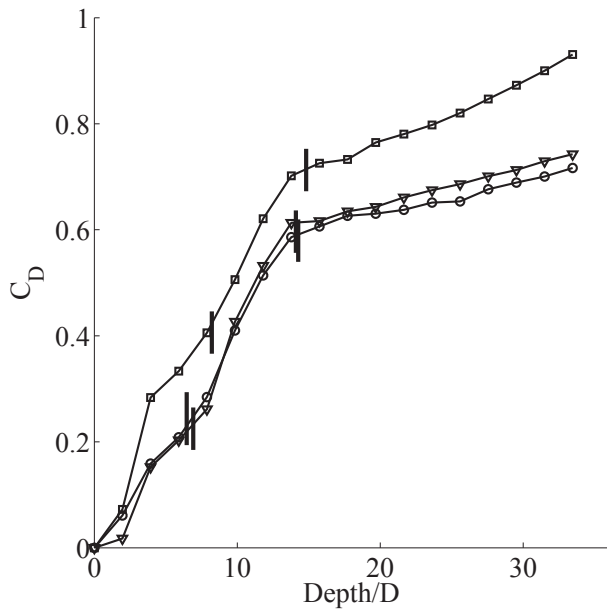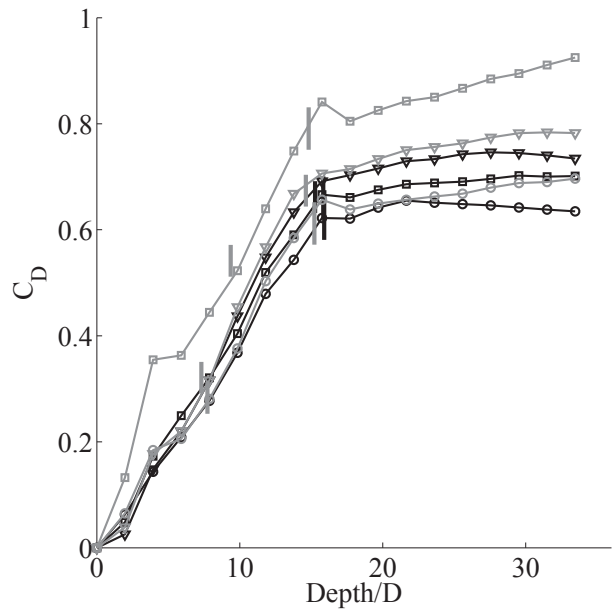
Figure 3.16: (a) Raw drag coefficient data for a hydrophilic cone overlaid with a third-degree polynomial fit line. (b) Mean of the drag coefficient for 10 runs each of hydrophilic (black) and hydrophobic (gray) cases. (c) Mean drag coefficient for half-and-half cases. (d) Mean drag coefficients for hydrophilic and hydrophobic 5° cases. Depth/D = 0 is impact with the free surface. The markers represent every 50 data points. The mean errors are (b) 0.03 (c) 0.02, and (d) 0.02. The maximum errors are (b) 0.09, (c) 0.18, and (d) 0.09. The vertical lines mark the mean pinch-off depths for the 10 tests of each nose.

Table 3.6: Total terminal velocities for each nose shape normalized by impact velocity.

Nose	Hydrophilic 0°	Hydrophobic 0°	Half-and-half	Hydrophilic 5°	Hydrophobic 5°
Cone	0.41	0.41	0.40	0.40	0.39
Ogive	0.53	0.52	0.51	0.54	0.52
Flat	0.45	0.42	0.41	0.47	0.41

3.3.4 Lift Coefficients

Lift is the component of the force that acts perpendicular to the direction of the fluid flow [28] and the lift coefficient is calculated by

$$C_L = \frac{2F_L}{\rho U^2 A} \tag{3.4a}$$

$$F_L = m_p a_L, \tag{3.4b}$$

where F_L is the lift component of the force, m_p is the mass of the projectile, a_L is the measured acceleration perpendicular to the relative fluid velocity, ρ is the density of the fluid, A is the frontal area of the projectile, and U is the velocity of the projectile through the water. The lift force causes the projectile to translate in the x direction and also contributes to the rotation seen in image sequence 3.2(c), (d), and (e).

Figure 3.17 presents the calculated instantaneous lift coefficients for the hydrophilic and hydrophobic 0° and 5° cases as well as the half-and-half case. Figure 3.17(a) shows that there is no significant lift force when the projectile descends straight down, as expected. Figure 3.17(b) shows a maximum lift coefficient of 0.21 for the flat nose shape in the half-and half case, with 0.2 and 0.05 for the ogive and cone, respectively. This finding corroborates the trajectory plots from figure 3.9, showing that the flat and ogive have more lateral displacement than the cone. The lift coefficients for the hydrophilic and hydrophobic 5° cases are shown in figure 3.17(c). The lift coefficients for both the hydrophilic and hydrophobic cone approach 1 and the lift coefficients for the hydrophilic cases for the ogive and flat are significantly larger than their respective hydrophobic lift coefficients. Comparing these values to trajectory plots in figure 3.4 shows that the hydrophilic and hydrophobic cone have essentially the same lateral displacement. The trajectories for the hydrophilic and hydrophobic cases for the ogive and flat in figures 3.4(b) and 3.4(c) achieve a

Table 3.7: Final lift coefficients obtained from figure 3.17

Nose	Hydrophilic 0°	Hydrophilic 0°	Half-and-half	Hydrophilic 5°	Hydrophobic 5°
Cone	0.04	0.03	0.10	0.84	0.84
Ogive	0.02	0.06	0.16	0.69	0.53
Flat	0.03	0.03	0.22	0.67	0.41

displacement of approximately 6 diameters. Figures 3.17(b) and 3.17(c) show a dip around 0.05 s which is due to the squared radial force components in equation 3.4b, similar to the discussion in section 3.2.3.

The final lift coefficient values for each nose and case are presented in table 3.7. The hydrophilic and hydrophobic 0° cases for all noses show almost no lift, and the half-and-half cases shows only a small amount. However, the 5° case for all noses shows a significant increase in the lift, which resulted in a proportional lateral displacement.

3.4 Acoustics

It is well known that the nose shape affects the formation of the cavity and splash curtain. However, there are still questions regarding the sounds produced during the water entry event. Using a hydrophone positioned 26 cm from the area of impact, the sounds produced by the three different nose shapes were recorded and processed and are represented in figure 3.19 as a spectrogram showing the intensity (color) of frequencies up to 48 kHz through time. Line A in figures 3.20(a) through 3.20(c) indicate the moment of impact. Line B represents the moment of pinch-off. The transition of the projectile from free-fall to impact with the water is obvious for the flat nose shape (figure 3.20(c)). However, the transition for the cone (figure 3.20(a)) and ogive (figure 3.20(b)) is very subtle and synchronization is necessary to determine the instant of impact. The spectrograms in figures 3.20(a) through 3.20(c) were computed from the waveform signal in figures 3.18(d), 3.18(e), and 3.18(f). Comparing the two sets of figures demonstrates that the spectrograms are well suited for observing sudden, dramatic changes in the signal, such as the flat impact or the pinch-off event for all three nose shapes. Additionally, comparing figure 3.18(i) with figure 3.19(f) shows how angling the projectile can be used to decrease the sound produced on
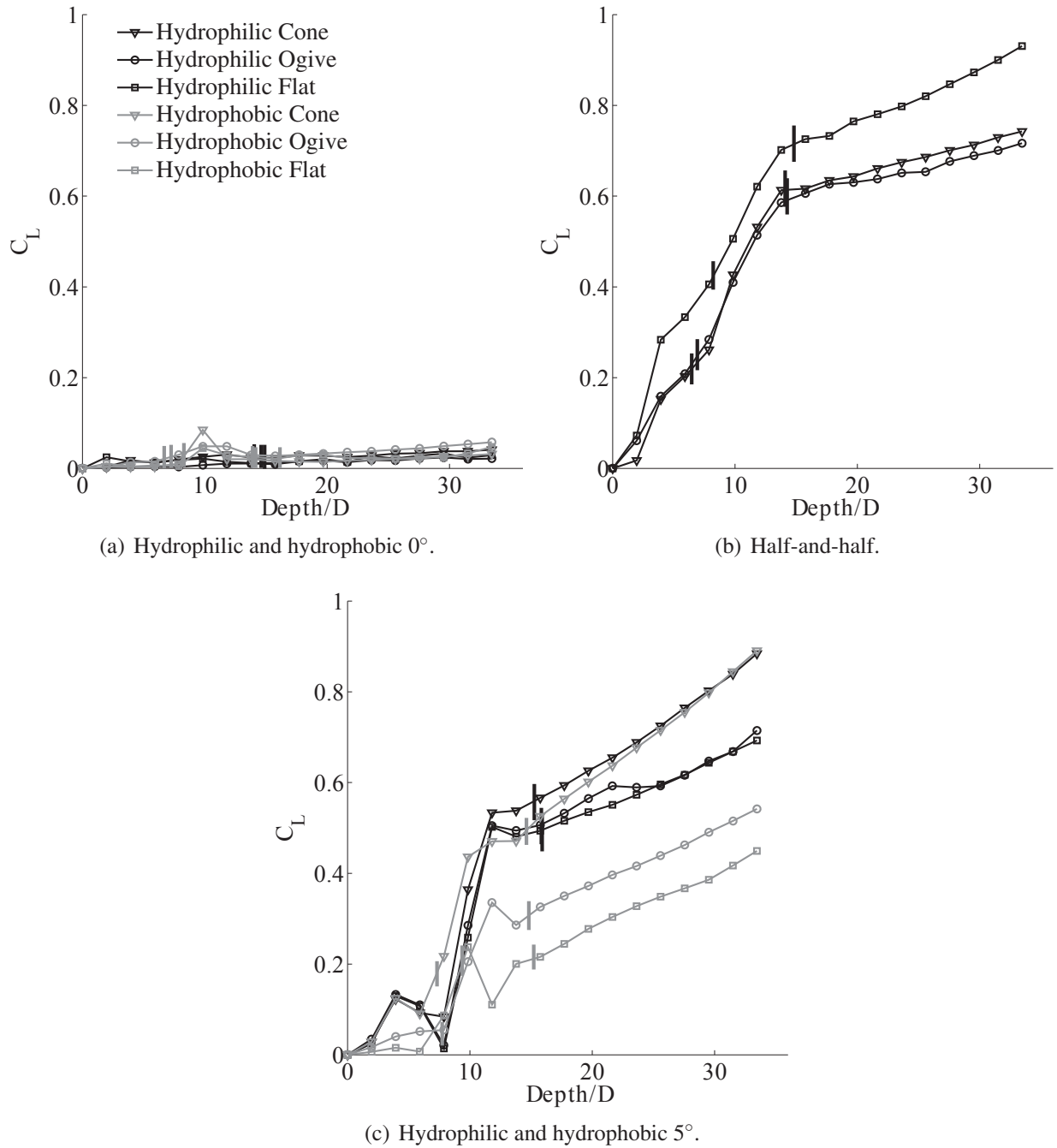
(a) Hydrophilic and hydrophobic 0°.

(b) Half-and-half.

(c) Hydrophilic and hydrophobic 5°.

Figure 3.17: (a) Hydrophilic and hydrophobic 0°. (b) Half-and-half. (c) Hydrophilic and hydrophobic 5°. Depth/D = 0 is impact with the free surface. The mean errors are (a) 0.02, (b) 0.04, and (c) 0.03. The maximum errors are (a) 0.09, (b) 0.22, and (c) 0.13. The dips in (b) and (c) around 0.05 s are caused by squaring the two radial acceleration values to compute the lift force, resulting in only positive values being shown. The vertical lines mark the mean pinch-off depths for the 10 tests of each nose.

impact for flat nose. Impact with the free surface at a 5° angle from vertical significantly decreased the sound produced.

Additional processing was required to compare the frequencies of the three nose shapes. Figure 3.20 shows the dominant frequencies calculated from impact until just before pinch-off for the three nose shapes for the cases of hydrophilic 0°, hydrophobic 0°, half-and-half 0°, and hydrophobic 5°. Each plot shows a dominant low frequency of approximately 200 Hz and the cone and ogive plots show other similar frequencies of 375 Hz, 1382 Hz and 2015 Hz. The amplitude values were normalized by the maximum value of the plots for each nose shape. The nearly identical frequency plots suggest that the sound produced by the formation of the cavity is independent of nose shape. However, figure 3.20 does show that the amplitude of the sound produced for each nose shape is affected by the wetting angle. The amplitudes of the dominant frequencies from the cavity-forming cases are very pronounced, while no frequency spikes are seen for the hydrophilic non-cavity-forming case.

3.4.1 Cavity Ripples

Figure 3.21(a) depicts an interesting phenomenon that is seen after pinch-off for all cases presented in this thesis. Ripples form on the sides of the bubble of entrained air behind the projectile, a phenomenon that has been previously studied by [16]. From the images, the time between successive ripples is found to be 5 ms. Acceleration data from the IMU show that at the corresponding time there are oscillations along the axial direction. The frequency of these oscillations is approximately 210 Hz, as shown in figure 3.22. The synchronized image-acceleration data (figures 3.21(a) and 3.21(b)) show that the ripples begin at pinch-off and decay through the remainder of the descent of the projectile. Continued oscillations are seen from the acceleration data, but obvious ripples are absent from the images after t = 0.155s. However, the IMU confirms that the sides of the trailing cavity continue to oscillate with a rippling pattern until the projectile impacts with the bottom of the tank ($t = 0.266$ s on figure 3.21(b); 35/D), a finding that cannot be observed from image data alone.

Figure 3.22 presents the frequencies of the 10 runs of each nose shape for hydrophilic cases from section 3.2.1 to the normalized amplitudes of each run. The mean frequencies for the cone, ogive, and flat nose shapes are 208.5 Hz, 210.9 Hz, and 212.7 Hz, respectively. Returning to the
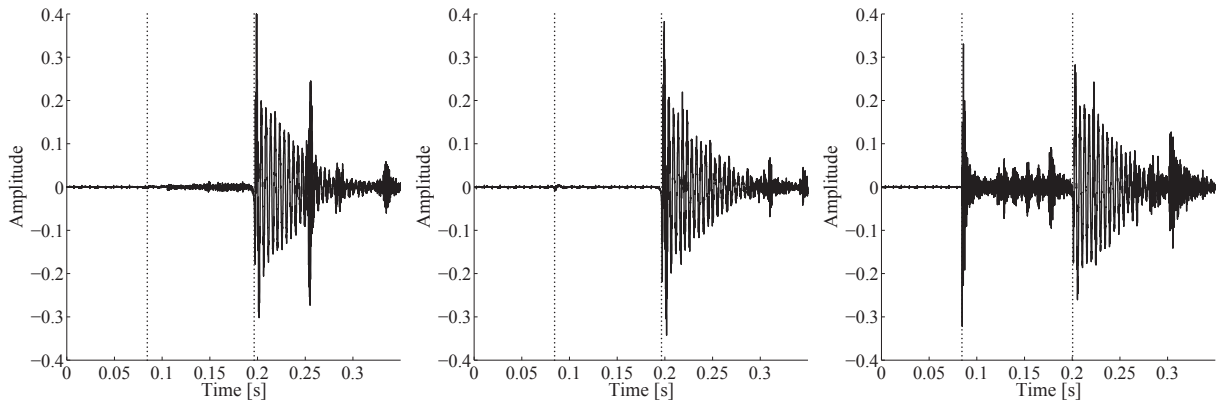
(a) Waveform of hydrophilic cone.   (b) Waveform of hydrophilic ogive.   (c) Waveform of hydrophilic flat.
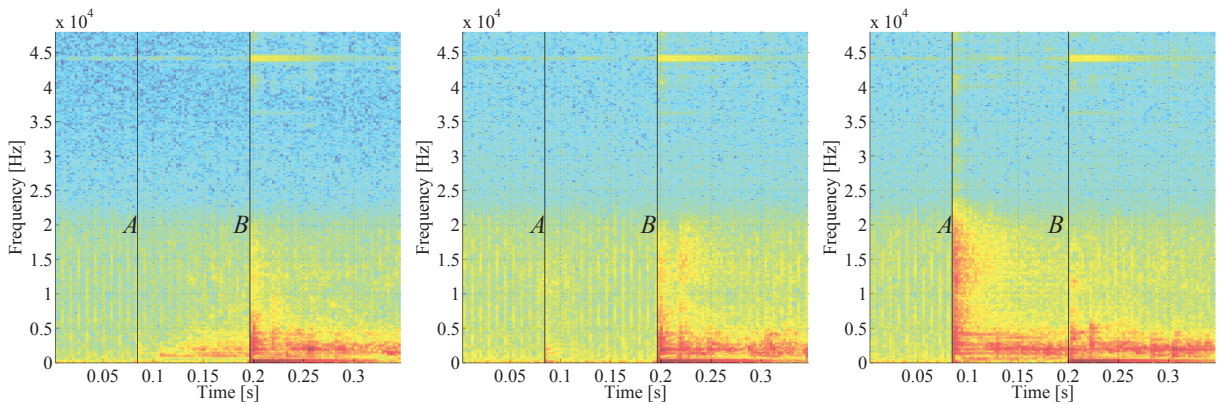
(d) Hydrophilic cone.   (e) Hydrophilic ogive.   (f) Hydrophilic flat.
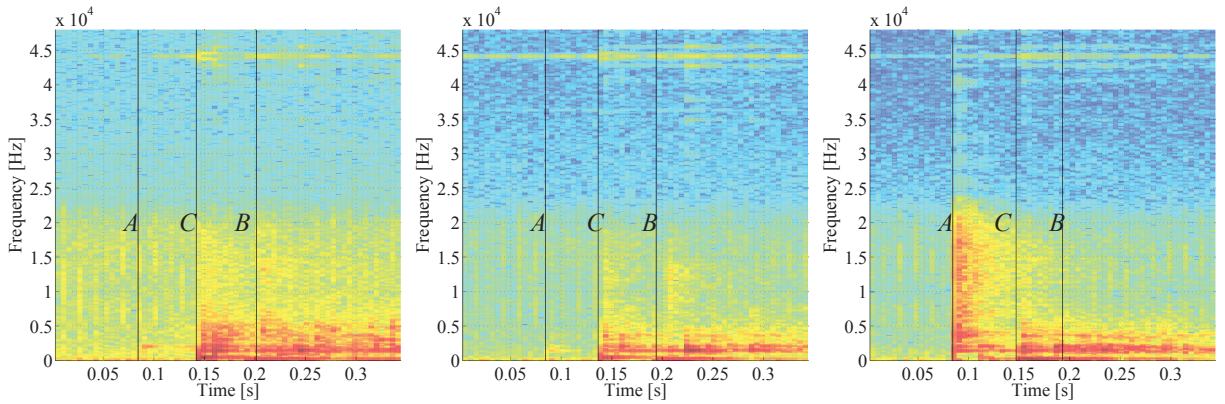
(g) Hydrophobic cone.   (h) Hydrophobic ogive.   (i) Hydrophobic flat.

Figure 3.18: Waveforms for the hydrophilic case are shown in (a), (b), and (c). Spectrograms for each nose shape for the hydrophilic and hydrophobic 0° cases are shown in (d) through (i). Dark red represent the strongest intensity values of the frequency at an instant in time. *A* and *B* represent the time of impact and pinch-off of the trailing cavity, respectively. The pinch-off for each case is similar to figure 3.2(a). Line *C* in (g), (h), and (i) represents the pinch-off of the cavity on the sides of the projectile, shown in figure 3.2(b). The spectrogram was computed using a Hanning window of size 512 with 250 samples of overlap.
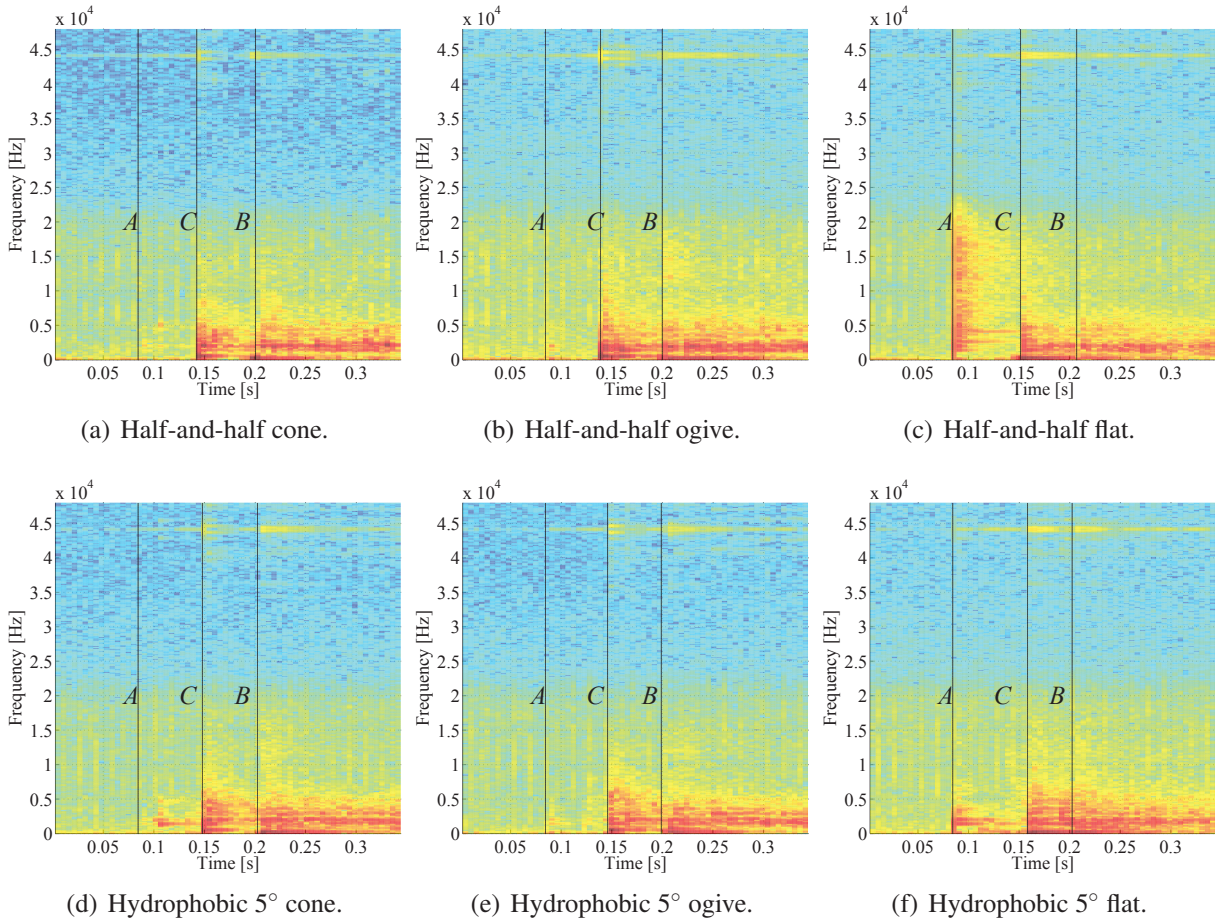
Figure 3.19: Spectrograms for each nose shape for the half-and-half case and hydrophobic 5° case. Dark red represent the strongest intensity values of the frequency at an instant in time. *A* and *B* represent the time of impact and pinch-off of the trailing cavity, respectively. Line *C* represents the pinch-off of the cavity on the sides of the projectile, shown in figure 3.2(c) and (e). The spectrogram was computed using a Hanning window of size 512 with 250 samples of overlap.

frequency plots from figure 3.20, the low dominant frequency of 200 Hz compares nicely with the acceleration frequency. Grumstrup et al. [16] showed oscillation frequencies of 190 Hz for spheres, and both the acoustic frequency and acceleration frequency are in the same range even for slender axisymetric projeciles.

3.5   Conclusion

This chapter presented results for trajectory, velocity, force, and acoustic effects of the water entry of slender axisymmetric bodies. A slender axisymmetric projectile will rotate and

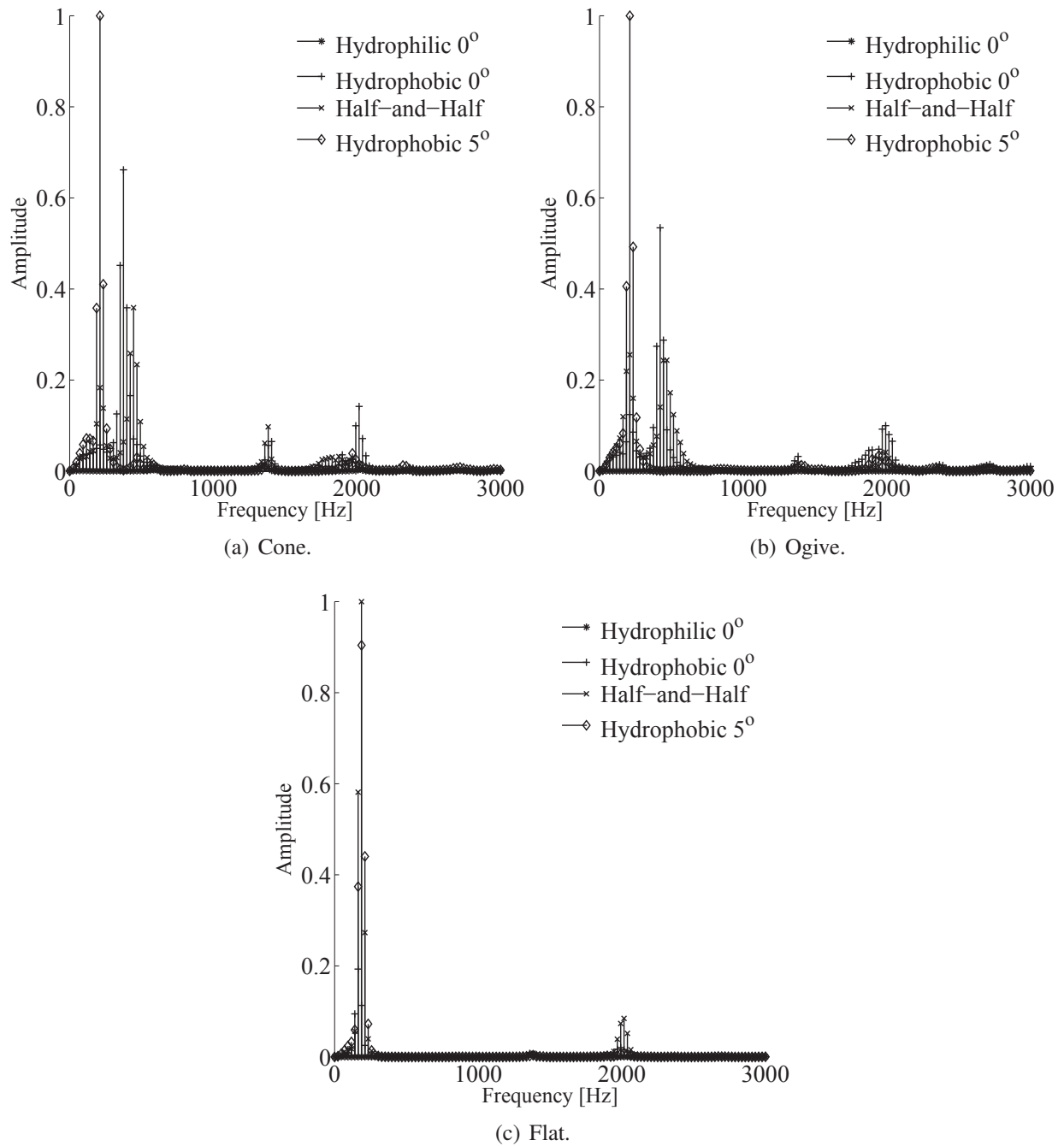(a) Cone.

(b) Ogive.

(c) Flat.

Figure 3.20: Dominant frequencies for cone, ogive, and flat nose shapes for the hydrophilic 0° and 5° case, half-and-half case, and hydrophobic 5° case. The frequencies above 3000 Hz provided no useful information.
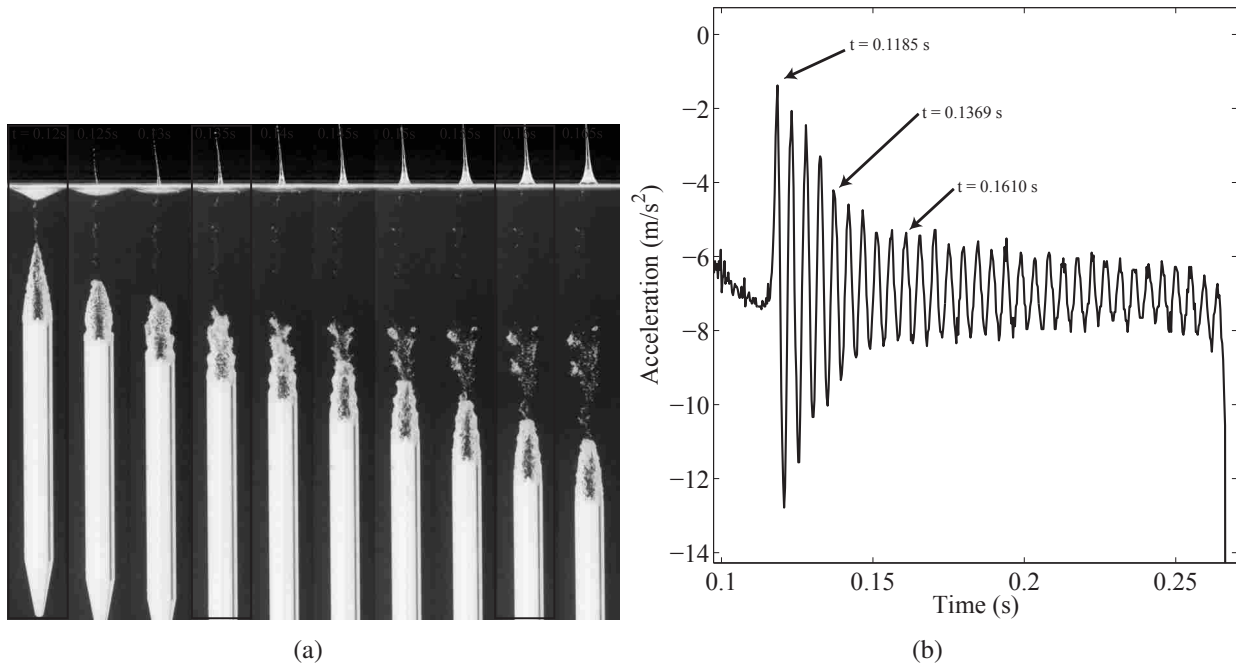
Figure 3.21: (a) Ripple formation and decay behind an aluminum cone with an impact velocity U_o ≈ 2.7 m/s and t = 5 ms. (b) Induced accelerations after pinch-off caused by the cavity rippling. The time is measure post-impact. The frequency of the oscillation is 212 Hz. The outlined images in (a) are the approximate times indicated in (b).
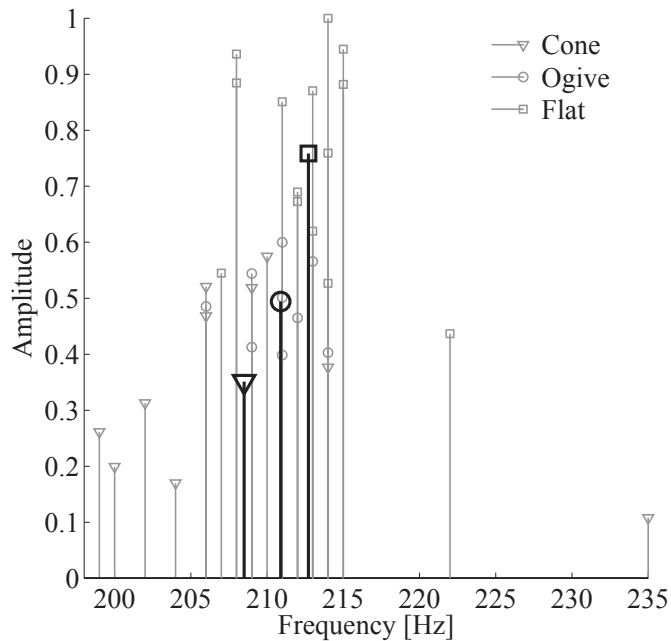
Figure 3.22: Ripple frequency of hydrophobic cases from acceleration data. The amplitudes were normalized by the largest value shown on the plot. The large dark markers represent the mean frequency and amplitude values for the cone, ogive, and flat nose shapes.

displace laterally if dropped at an oblique angle as well as if coated such that an asymmetric cavity is created on impact. However, the oblique entry cases showed significantly more lateral translation than the asymmetric cavity (half-and-half) cases. The impact force for the flat nose was approximately 10 times greater than for the cone or ogive nose shapes. Instantaneous lift and drag coefficients were calculated for all cases. Audio spectrograms showed differences in time between the hydrophilic and hydrophobic cases.

CHAPTER 4.   CONCLUSIONS

This thesis presented trajectory, force, and acoustic findings for slender axisymmetric projectiles with three nose shapes and three surface coating conditions, entering the water vertically and at oblique angles. An embedded inertial measurement unit (IMU) was used to measure accelerations from which the forces, velocities, and positions were calculated and compared.

4.1   Summary of Trajectory & Velocity Results

The acceleration data from the IMU were integrated to obtain velocities and positions for the entire water entry event. The calculated positions showed a larger lateral displacement for the oblique entry cases than for the half-and-half coated case. The hydrophobic coating caused a cavity to form at impact and resulted in increased drag and decreased velocity compared to the hydrophilic case. The effect of adjusting the center of mass of the test projectile was shown, resulting in greater lateral displacement as the center of mass was moved farther from the nose of the projectile, as predicted. Finally, non-dimensional pinch-off times were calculated and compared to a previous study with good agreement.

4.2   Summary of Force Results

Impact forces were calculated for the cone, ogive, and flat nose shapes for four cases. The flat showed the largest impact force in the vertical entry cases, which was lessened during oblique water entry cases. The wetting angle does not significantly affect the impact force, but the nose shapes has a drastic effect. Drag and lift coefficients were computed for four cases and showed that the lift force was responsible for the lateral displacement seen in the trajectory plots.

4.3 Summary of Acoustics Results

A spectrogram was calculated from synchronized acoustic data that showed that the majority of the sound produced by the cone and ogive nose shapes was a result of pinch-off and not from the actual impact with the free surface. The flat nose for both hydrophilic and hydrophobic cases produce an intense sound at impact and less sound at pinch-off. In addition, the impact sound for the flat nose can be reduced by entering the water at an oblique angle. Acoustic and acceleration frequency data agreed well with ripple frequency findings previously studied by other researchers.

4.4 Future Work

A principal area of focus for future work is to further refine the use of the IMU, especially to reduce the error associated with the hardware. The first item to implement would be a Kalman filter, which was not used in this thesis. Secondly, the hardware components should be updated as faster, more precise accelerometers and gyroscopes become available.

There are many other studies that can be performed using the IMU to acquire data. One such study already underway is the skipping of a Waboba ball on the water. Studies using variations in the type of nose shapes as well as the dimensions of the shapes, especially the cone, used in this thesis could be performed to further understand how other nose shapes are affected by the half-and-half coating and oblique entry. Also, instead of using rigid noses, flexible nose water entry tests could be conducted to study the effect of non-rigid nose shapes on impact forces, asymmetric cavity formation, and sound production. Larger entry angles and their effect on projectile trajectories could also be studied specifically looking for threshold angle beyond which the trajectory is not controlled. Particle image velocimetry (PIV) studies to determine the effects of the long body on vortex shedding would be instructive. Additionally, using PIV to observe the air-water interface of the trailing cavity would provide insight into the formation and decay of the ripple effect.

Numerical studies focused on predicting the trajectory and velocity of a projectile in the half-and-half case or the oblique entry case could be performed to compare with the findings from the IMU. Additional work with the acoustics to further refine frequency signatures could be performed as well.

REFERENCES

[1] May, A., Baldwin, J. L., Walker, W. A., and Goeller, J. E., 1979. Hydroballistics design handbook volume i Tech. Rep. SEAHACTR79-1, Naval Sea Systems Command Hydromechanics Committee. 1, 6

[2] Gekle, S., Gordillo, J. M., van der Meer, D., and Lohse, D., 2009. "High-speed jet formation after solid object impact." *Phys.Rev.Lett.,* **102**(3), Jan, p. 034502. 2, 5

[3] Truscott, T. T., Epps, B. P., and Techet, A. H., 2012. "Unsteady forces on spheres during free-surface water entry." *Journal of Fluid Mechanics,* **704**, p. 173. 2, 3, 6, 42

[4] Duez, C., Ybert, C., Clanet, C., and Bocquet, L., 2007. "Making a splash with water repellency." *Nat Phys,* **3**(3), print, pp. 180–183 M3: 10.1038/nphys545; 10.1038/nphys545. 2, 5, 6

[5] Worthington, A. M., and Cole, R. S., 1897. "Impact with a liquid surface, studied by the aid of instantaneous photography." *Philosophical Transactions of the Royal Society of London.Series A, Containing Papers of a Mathematical or Physical Character,* **189**, pp. pp. 137–148. 4

[6] Worthington, A. M., 1908. *A study of splashes*. Longmans, Green, and Co., London. 4

[7] Duclaux, V., Cailla, F., Duez, C., Ybert, C., Bocquet, L., and Clanet, C., 2007. "Dynamics of transient cavities." *Journal of Fluid Mechanics,* **591**, p. 1. 4, 6

[8] Aristoff, J. M., Truscott, T. T., Techet, A. H., and Bush, J. W. M., 2010. "The water entry of decelerating spheres." *Physics of Fluids,* **22**(3), March 2010, p. 032102. 4, 5, 6

[9] Gilbarg, D., and Anderson, R. A., 1948. "Influence of atmospheric pressure on the phenomena accompanying the entry of spheres into water." *Journal of Applied Physics,* **19**(2), February 1948, pp. 127–139. 4

[10] Nesteruik, I., 2004. "Subsonic shapes without separation and cavitation." *Mechanics of 21st Century - ICTAM04 Proceedings*. 5

[11] Lee, M., Longoria, R. G., and Wilson, D. E., 1997. "Cavity dynamics in high-speed water entry." *Physics of Fluids,* **9**(3), March 1997, pp. 540–550. 5

[12] Bergmann, R., Meer, D. V. D., Gekle, S., Bos, A. V. D., and Lohse, D., 2009. "Controlled impact of a disk on a water surface: cavity dynamics." *Journal of Fluid Mechanics,* **633**, p. 381. 5, 6

[13] Techet, A. H., and Truscott, T. T., 2011. "Water entry of spinning hydrophobic and hydrophilic spheres." *Journal of Fluids and Structures,* **27**(56), 0, pp. 716–726. 5, 6

[14] Uber, B. D., and Jr, R. J. F.", 1973.." *Acoustic signatures accompanying low-velocity water entry*. 5

[15] Honghui, S., and Makoto, K., 2004. "Underwater acoustics and cavitating flow of water entry." *Acta Mechanica Sinica,* **20**(4), 08/01, pp. 374–382 J2: Acta Mech Sinica. 6

[16] Grumstrup, T., Keller, J. B., and Belmonte, A., 2007. "Cavity ripples observed during the impact of solid objects into liquids." *Physical Review Letters,* **99**(11), 09/12, p. 114502 ID: 10.1103/PhysRevLett.99.114502; J1: PRL. 6, 65, 67

[17] Baldwin, J. L., 1971. "Vertical water entry of cones.". 6

[18] Moghisi, M., and Squire, P., 1981. "An experimental investigation of the initial force of impact on a sphere striking a liquid surface." *Journal of Fluid Mechanics,* **108**, pp. 133–146. 6, 7

[19] Xu, G. D., Duan, W. Y., and Wu, G. X., 2011. "Numerical simulation of water entry of a cone in free-fall motion." *The Quarterly Journal of Mechanics and Applied Mathematics,* **64**(3), August 01, pp. 265–285. 6

[20] Jr, A. B. W., Morrison, A. M., and Baldwin, J. L.", 1977.." *Prediction of Impact Pressures, Forces, and Moments During Vertical and Oblique Water Entry*. 6

[21] Shiffman, M., and Spencer, D., 1951. "The force of impact on a cone striking a water surface (vertical entry)." *Communications on Pure and Applied Mathematics,* **4**(4), pp. 379–417. 6

[22] Battistin, D., and Iafrati, A., 2003. "Hydrodynamic loads during water entry of two-dimensional and axisymmetric bodies." *Journal of Fluids and Structures,* **17**(5), pp. 643–664. 6

[23] Oliver, J. M.", 2002.." *Water entry and related problems*. 6

[24] Backer, G. D., Vantorre, M., Beels, C., Pr, J. D., Victor, S., Rouck, J. D., Blommaert, C., and Paepegem, W. V., 2009. "Experimental investigation of water impact on axisymmetric bodies." *Applied Ocean Research,* **31**(3), 7, pp. 143–156. 7

[25] Lewis, S. G., Hudson, D. A., Turnock, S. R., and Dominic, J., 2010. "Impact of a free-falling wedge with water: synchronized visualization, pressure and acceleration measurements." *Fluid Dynamics Research,* **42**(3), p. 035509. 7

[26] Jenoptik. Hommel Tester T8000. http://http://www.agil-technologies.com/roughness.php. 12

[27] Hommelwerke, 2003. Hommel Tester T8000 Technical specifications. Hommelwerke. 12, 13

[28] Cengel, Y. A., and Cimbala, J. M., 2010. *Fluid Mechanics: Fundamentals and Applications.,* second ed. McGraw-Hill, New York. 17, 58, 62

[29] Maynes, D. *Intermediate Fluid Mechanics*. BYU Academic Publishing. 17

[30] ADXL345. http://www.sparkfun.com/datasheets/sensors/accelerometer/adxl345.pdf. 20

[31] ITG-3200. http://www.sparkfun.com/datasheets/sensors/gyro/ps-itg-3200-00-01.4.pdf. 20

[32] Baruh, H., 1999. *Analytical dynamics*. WCB/McGraw-Hill Boston. 28

[33] H2a hydrophone user's guide. http://www.aquarianaudio.com/aqauddocs/h2a_manual.pdf. 33

[34] Alexander, C. K., and Sadiku, M. N. O., 2009. *Fundamentals of Electric Circuits*. McGraw-Hill, New York. 34

[35] Truscott, T. T., and Techet, A. H., 2009. "Water entry of spinning spheres." *Journal of Fluid Mechanics,* **625**(1), pp. 135–165. 55